ABSTRACT

MODELING, DESIGN, AND FABRICATION OF PULSED FLUIDIC MICRO-ACTUATORS

by
Max Roman

The forced vibration of a thin flexible plate or membrane in a sealed cavity with a small opening can cause fluid to be pumped into and out-of the cavity. At particular frequencies and amplitudes of vibration, a streaming of vortex rings can occur near the orifice. These vortex rings move under their own self-induced momentum. Downstream of the opening the rings ultimately break up and can form a fully developed jet. This work is dedicated to the analysis, design, and fabrication of electrostatic micro fluidic actuators, which use the pulsing mechanism described above to generate a fluid flow. Particle Image Velocimetry (PIV) is used to visualize the jet at various drive frequencies. The complex coupling between the electric field driving the membrane, the deformation of the membrane, and the compressible squeeze film in the cavity are studied in depth. Theoretical modeling, computer simulation (CFD-Computational Fluid Dynamics) and experiments are used to characterize the performance of the actuator. A low dimensional theoretical model, which takes into account the coupled physics of the problem, is derived from the Newton equation. The model is used to predict the membrane motion for varying voltage and frequency inputs. The system response predicted with the model is compared to numerical simulations, and it was found that the model can accurately capture the system response for a given input. Finally, a protocol for fabricating the actuator using Micro Electrical Mechanical Systems (MEMS) processes is presented.

MODELING, DESIGN, AND FABRICATION OF PULSED FLUIDIC MICRO-ACTUATORS

by
Max Roman

A Dissertation
Submitted to the Faculty of
New Jersey Institute of Technology
in Partial Fulfillment of the Requirements for the Degree of
Doctor of Philosophy in Mechanical Engineering

Department of Mechanical Engineering

January 2006

APPROVAL PAGE

MODELING, DESIGN, AND FABRICATION OF PULSED FLUIDIC MICRO-ACTUATORS

Max Roman

Dr. Nadine Aubry, Dissertation Advisor — Date
Distinguished Professor of Mechanical Engineering, NJIT

Dr. Pushpendra Singh, Committee Member — Date
Professor of Mechanical Engineering, NJIT

Dr. Denis L. Blackmore, Committee Member — Date
Professor Mathematical Sciences, NJIT

Dr. I. Joga Rao, Committee Member — Date
Associate Professor of Mechanical Engineering, NJIT

Dr. Suresh Goyal — Date
Distinguished Member of Technical Staff, Bell Labs Research

BIOGRAPHICAL SKETCH

Author: Max Roman

Degree: Doctor of Philosophy in Mechanical Engineering

Date: January 2006

Undergraduate and Graduate Education:

- Doctor of Philosophy in Mechanical Engineering,
  New Jersey Institute of Technology, Newark, NJ, 2006
- Master of Science in Mechanical Engineering,
  New Jersey Institute of Technology, Newark, NJ, 2001
- Bachelor of Science in Mechanical Engineering,
  New Jersey Institute of Technology, Newark, NJ, 2000

Major: Mechanical Engineering

Presentations and Publications:

Bao, Z., Mukherjee, S., Roman, M. and Aubry, N., "Nonlinear Vibrations of Strings and Membranes without Tension", ASME Journal of Applied Mechanics 71(4), 551-559, 2004.

Bao, Z., Mukherjee, S., Roman, M. and Aubry, N., "Nonlinear Mechanics of MEMS Plates with a Total Lagrangian Approach." Computers and Structures. Volume 83, Issues 10-11, April 2005, pp. 758-768.

Roman, M. and N. Aubry, "Design and Fabrication of Electrostatically Actuated Synthetic Microjets." ASME Paper No. IMECE2003-41579. New York: American Society of Mechanical Engineers; 2003.

I dedicate this work to all members of my family and to my close friends, past and present. May this work serve as inspiration to accomplish your goals.

ACKNOWLEDGEMENT

I would like to thank my advisor, Dr. Nadine Aubry, for all her guidance and support throughout the course of this work. She has been not only a mentor, but an inspiration to continuously challenge and push myself. I feel privileged to have had the opportunity to work with her. I would also like to thank my committee members, Dr. Pushpendra Singh, Dr. Denis Blackmore, Dr. Joga Rao, and Dr. Suresh Goyal for their input and critique of this work. I am especially grateful for their patience and understanding when I continuously fell behind schedule. I must also extend my gratitude to Arnaud Goullet, who has been more like a co-advisor as well as a great friend. Thank you for spending all those late nights in the lab with me, discussing ideas and results.

I also thank Ed Kleissler, who has been extremely supportive throughout my graduate studies. He has been both a great friend and mentor to me. His enthusiasm for new ideas is staggering and contagious. I must also extend a great thank you to Ms. Sharyn Sarafin. I feel extremely fortunate to have worked with her. If not for the efforts of Eric Bower at Lucent Bell Labs, the microjet would never have been completed. Thank you for the support long after the funding ran out.

I would like to thank all the PhD students with whom I have had the pleasure of working with. I would especially like to extend a thank you to Amit Banerjee and Shriram Pillapakam. I am certain that the friendship that we have forged will last a lifetime. Finally, I thank the faculty of the Mechanical Engineering department, with whom I have now spent a good deal of my life with and am better for it.

TABLE OF CONTENTS

TABLE OF CONTENTS
(continued)

Chapter **Page**

LIST OF FIGURES

Figure **Page**

LIST OF FIGURES
(continued)

Figure **Page**

LIST OF FIGURES
(continued)

Figure **Page**

LIST OF TABLES

Table **Page**

CHAPTER 1

INTRODUCTION, OBJECTIVES, AND OUTLINE

1.1 Introduction

The subject of flow control is of immense technological interest and accounts for a large area of today's current research in fluid mechanics. The goal of such study is to reduce drag, increase lift, suppress vortex shedding and flow-induced noise, enhance mixing, filtration, or any other desirable effect. Numerous control schemes aimed to favorably alter the characteristics or natural inclination of a flow field have been suggested and implemented with varying degrees of success. Some control tools for wall bounded flows include the application of compliant coatings, suction or injection, electromagnetic forces (in conducting fluids), heating and cooling, and the addition of shear thinning or thickening additives into the boundary layer (7). All of these methods are designed to alter the instantaneous and mean velocity profiles and lead to the desired flow control effect.

Recent advances in microfabrication offer the opportunity and framework to build inexpensive, reliable, light weight, low power actuators and sensors that have the potential of curtailing the penalties and drawbacks associated with conventional flow controlling schemes, such as response time, size and weight, cost, and durability. Before any rewards are to be reaped from such small-scale devices and any significant large scale application of these devices is to take place, much more data is required. In addition, as the fluid behavior at small scales itself is still not well understood, optimization of the devices themselves has hardly been addressed. Current design is

based not on optimal flow characteristics, but rather on simplicity of fabrication using standard microfabrication techniques.

Proposed herein is the concept, design, and fabrication of an actuator that by creating a fluid jet could potentially be used in various flow controlling schemes. A cross-sectional drawing of the proposed device is shown in Figure 1.1.

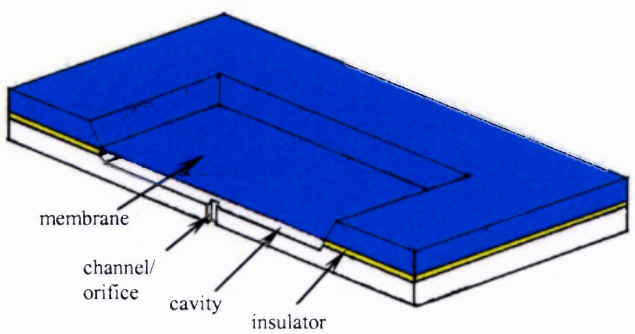

Figure 1.1 Three-Dimensional cut-out view of a Micro Electro Mechanical System (MEMS) jet.

The jet is generated by the oscillation of a membrane in a cavity that is sealed, except for a small orifice on one face of the cavity. A key feature of the synthetic jet is that it can be readily microfabricated. From a fabrication and application point of view, the synthetic jet is attractive in that no external tanks, valves, pipes, or pumps are necessary to create the jet flow. The jet is synthesized, hence its name, from the surrounding fluid. A synthetic jet has zero-net mass flux. That is, with each cycle, the surrounding fluid is sucked into a sealed cavity and then expelled outward through an orifice into the same surrounding fluid. No additional fluid is added from an external

source outside of the domain. The amount of fluid exiting through the orifice is equal to the amount of fluid entering through the orifice. A very simple synthetic jet can be fabricated using a speaker mounted in a sealed cavity with a small opening on its opposite end.

Though seemingly simple in concept, a synthetic jet is quite a complex system to analyze. The jet flow can essentially be split into two primary domains: the internal and external fluid regions. The fluid flow inside the cavity is a result of a coupled interaction between the oscillating membrane and the fluid. There is a further coupling between the external force applied to the membrane and the membrane itself. Usually, the external driving force comes from an electric field, such as electrostatic or piezoelectric actuation. In practice, it is difficult to decouple the driving frequency and stroke, or maximum membrane amplitude, of the actuator. A key element, then, is to minimize the voltage and power required to drive the membrane. In a MEMS scaled system, which is characterized by very large lateral dimensions relative to the height of the cavity, the squeeze film problem must also be considered, as it can have significant damping and stiffness effects on the membrane itself. The amount of spring or damping is a function of the driving frequency of the membrane. It is difficult to physically measure and visualize the flow inside the cavity, therefore modeling tools are very useful in analyzing the fluid flow there.

The external domain is bounded at the exit plane of the jet. At particular frequencies and amplitudes of excitation of the membrane, as the fluid passes through the opening, a train of vortex rings is created at the edges of the orifice. The vortex pairs

characterize the near field evolution of the synthetic jet. These counter-rotating vortex pairs are carried outward under their own self induced momentum, as illustrated in

Figure **1.2**). In the far field, the individual vortex rings break apart and eventually coalesce into a fully developed jet (9). Figure 1.3 displays the experimental visualization of a synthetic jet evolving near the orifice with the formation of a roll-up of vortices, which develop into a turbulent jet further downstream.

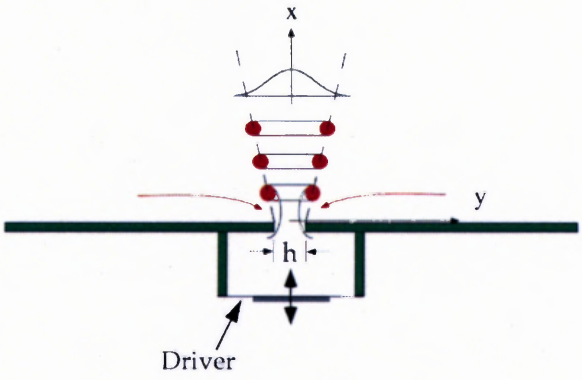

Figure 1.2 Concept of a synthetic jet.

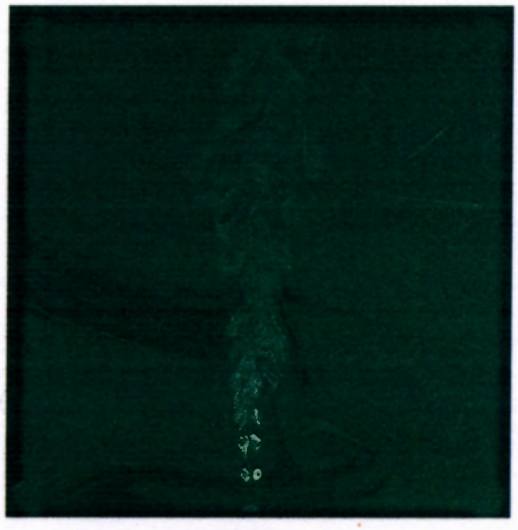

Figure 1.3 Flow visualization of synthetic jet. (Roman 2004)

Jet flows created by vibrating plates in sealed cavities having a small opening have been studied experimentally using Schlieren images, hot wire anemometry, and PIV (Particle Image Velocimetry) techniques. Some numerical modeling has also been conducted to study both the flow inside the cavity as fluid is drawn in, and outside the cavity, downstream beyond the opening. (18,12). Wang and Menon (25) numerically explored the use of synthetic microjets for fuel-air mixing enhancement. Although insightful, most of the numerical studies attempting to characterize synthetic microjets do not accurately represent the boundary conditions and geometries that are a result of microfabrication. In particular, these studies do no account for the large aspect ratios which result in very high fluid pressures inside the cavity at high actuation frequencies.

While the concept is not necessarily new, the aggressive study and development of synthetic jets is a rather recent field. Much of the work on synthetic jets has been spearheaded and centered around Ari Glezer's group at Georgia Tech. Coe and Glezer (5) published the first paper on microfabrication of synthetic jets. Their seminal paper is still frequently referenced, for having indicated the feasibility and practicality of synthetic microjet designs. More recently, Michael Muller at the University of Michigan has been actively pursuing the synthetic microjet concept applied to thrust generation for micro flying devices (13,14,15). However, although promising, the study is still very much in its infancy.

Due to their size and low power consumption, there are many appealing applications for synthetic microjets, ranging from thermal cooling of electronics and vectoring of larger jet flows to turbulent flow control and mixing. In addition, with some

modification, the synthetic jet concept can be extended to the design of micropumps for use in microfluidic delivery systems (28, 29), fuel atomizers, and for printheads.

There are several reasons why it makes sense to microfabricate synthetic jets. Due to their size, microfabricated devices are lightweight, require minimal space, can be batch fabricated for low cost and improved reliability, and impose very low power requirements. Batches of these microdevices can be connected to form larger arrays, which can be addressed individually or in clusters. Since they are batch produced, the batches would have very consistent geometric tolerances and properties. The increase in surface area to volume ratio inherent to microdevices makes them very efficient for their size, requiring very little power (milliwatt range) to operate. Additionally, as the scale decreases, the acoustic frequency increases, which results in a higher operating Reynolds number. In addition, the integration of MEMS-scale jet actuators and sensors distributed over a large control area can be envisioned for optimal flow control.

1.2 Objectives

For the purpose of this work, several objectives have been set. The subject of synthetic jets is still an emerging field. In particular, the works of Glezer (8,9) have shown that the flows generated by pulsing jets can have a significant influence on larger flow fields, as was previously discussed in the introduction part of this chapter. However, these flows are still poorly understood. It is clear that the direct cause of the vortex rings that are created at the exit are caused by flow separation at the sharp edges; however, the evolution of these vortex rings, how they originate in the cavity, and how they are created

by the oscillation of the membrane, is much less understood. Chapter 2 of this work deals specifically with flows generated by synthetic jets.

Another area which deserves attention is a thorough analysis of the fully coupled (actuation, membrane displacement, fluid flow) synthetic jet actuator. It has been common practice to simply build a device and then apply it to some flow. However, many synthetic jet actuators that work well in the lab environment do not operate as intended when scaled up or used in a real-world flow control situation. Therefore, it is this thesis's goal to attempt to fully analyze the problem and its dependence on the various parameters involved. Once the role of all parameters is known, the likelihood that the actuator will work as intended is far greater. Chapters 3 through 6 deal with this issue and serve as the main body of this work, the main objective being to derive a reduced model, a set of closed equations, that can facilitate and speed-up the design of microjets. The closed equations are easier to use and can offer more insight into the problem than full numerical simulations.

For a number of years, many experts on flow control, such as Gad-el-Hak (7), have pointed to MEMS as primary elements in flow controlling schemes. Without a doubt, MEMS sensors, such as pressure sensors and accelerometers, have been very successful. However, MEMS actuators have not shared the same degree of success in the control of fluid flows. Coe et al. (5), for instance, indicate that synthetic microjets can be viable flow control actuators, but yet, many details are lacking. The final goal is to fabricate a synthetic microjet actuator which can be shown to function as intended, that is, causing the fluid, air, to flow at a certain speed and flow rate for a given membrane oscillation. The final chapter deals with the fabrication of a microjet using MEMS

fabrication techniques. Having laid the foundation, it is hoped that the design and device developed here can set the stage for future work on synthetic microjets. With the successful operation of the actuator the next phase of research will focus on the jet flow generated by the actuator and its interaction with a larger flow for the control of the latter.

1.3 Outline

In Chapter 2, the synthetic jet concept is established experimentally. A miniature synthetic jet is fabricated using conventional machining processes, and flow fields created by the actuation of this jet are presented. Particle Image Velocimetry (PIV) is used to illuminate and visualize the flow field, and flows for varying actuating frequencies are shown. Some tests are conducted using the jet to cool electronic components, and the results are presented here.

Having established the concept, chapter 3 focuses on the mechanics of the membrane, which drives the fluid in a synthetic jet. A detailed analysis using energy methods for the large deformation of membranes is presented. In particular, an analytical expression relating pressure to deformation (for large deformations) is derived. The first part of the chapter deals particularly with square and rectangular membranes, which are common geometries resulting from typical MEMS fabrication processes. The second part of the chapter deals specifically with circular membranes. The last section of the chapter presents the dynamic analysis of membranes. Specifically, an analytical solution for the natural frequency of membranes subject to large deformations is derived. Throughout the chapter, results using the analytical expressions are compared to those obtained numerically, primarily with the use of ANSYS.

The electrostatic actuation is discussed in chapter 4. The chapter begins with a review of the parallel plate capacitor. This is followed with a detailed analysis of the membrane capacitor, for both small and large deflections. The objective is to derive analytical expressions which can predict the membrane deflection as a function of the applied voltage. The derived expressions also predict the gap distance when the system becomes unstable and pull-in occurs. The pull-in behavior is then further studied using ANSYS Multiphysics, which solves the coupled electric field - structure interaction problem. Results from the simulations are compared with the analysis. A means for estimating the electrical power required to put the membrane into motion is also included.

Chapter 5 is dedicated to the study of the fluid flow in the cavity. A brief discussion on Helmholtz resonators introduces the chapter. In the following section, the fluid is analyzed as an incompressible fluid. The continuity equation is applied to arrive at some estimate of the fluid velocity at the orifice of the jet. A low dimensional model is employed next to account for the compressibility of the fluid. The result is a coupled set of ODEs describing the pressure in the cavity and the fluid exit velocity as functions of time. Solutions to the ODEs are compared to those obtained with FLUENT. Lastly, the fluid flow is studied more rigorously using the compressible Reynolds equation for squeeze films. The Reynolds equation is solved analytically with MATLAB and numerically with a PDE solver. The damping and stiffness coefficients are derived. The coupled squeeze-film / fluid-structure interaction is also studied numerically using ANSYS. The results are also compared to the analytical expressions.

The fully coupled system with the electric field - structure - fluid interaction is addressed in Chapter 6. To this end, the equation of motion is applied, using the forces

derived in the previous three chapters, as inputs. The damping and stiffness coefficients from the squeeze film analysis are applied here. A low order model is then derived which captures the important features of the dynamics of the system. Namely, the membrane position is determined by inputting the primary parameters of the problem, such as the drive voltage and frequency. The fully coupled problem is also solved using ANSYS Multiphysics and results are compared to those obtained with the model.

Using insight gained through the analysis, a protocol for fabricating synthetic microjets is presented in Chapter 7. Steps for fabricating the device using microfabrication processes are outlined in detail. Images of the fabricated devices are shown.

In the last chapter, a brief summary is given and directions for future work are proposed.

CHAPTER 2

EXPERIMENTAL RESULTS

2.1 Experimental Set-up

As a starting point for understanding the fundamental fluid flow generated by a synthetic jet actuator, a miniature synthetic jet was fabricated using conventional machining techniques. The driver is a 25 mm diameter speaker. The cavity, which is 4mm high, is machined from aluminum. The speaker is mounted to the bottom of the cavity, and a 2 mm thick plate is mounted on the top, thus closing off the cavity. A 3 mm diameter hole was machined in the center of the top plate. Dimensions and construction are shown in Figure 2.1. The entire unit is clamped together using screws around the circumference, thus ensuring a sealed fit. The speaker is connected to a sine wave function generator with a 20 Volt power supply.

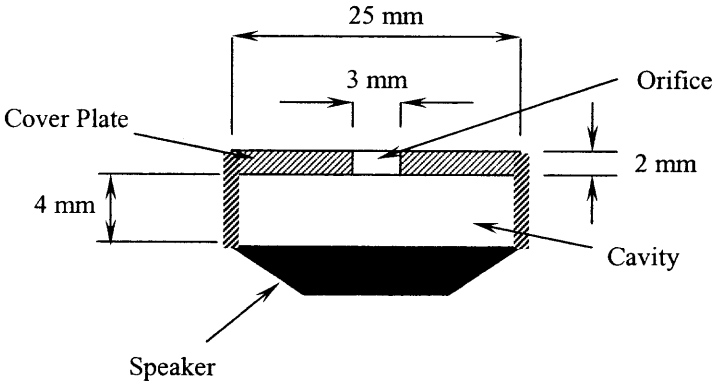

Figure 2.1 Synthetic Jet actuator construction and dimensions.

To visualize the flow, the entire unit was mounted to a board and fitted to the empty wall of a large fish tank. On the backside of the board, channels were fabricated that could allow smoke from an incense stick to flow through. The smoke from the incense first rose through the channels in the board, and was subsequently entrained by the jet as it exited the orifice. A class IV PIV laser was used to illuminate the plane through the flow field of the jet. Consecutive snapshots were taken at a rate of 30 frames per second with a camera. The excitation frequency of the jet was varied in a band between 500 – 3800 Hz. Outside of this range no jet was observed.

2.2 Flow Visualization

Throughout the published literature (8,9,16), it is reported that a single jet is observed at a frequency relating to the resonant frequency of the driver. However, in the author's observations, distinctly defined jets were seen to develop at frequencies well outside the driver's resonant frequency.

a. 600 Hz

b. 700 Hz

c. 800 Hz

d. 1200 Hz

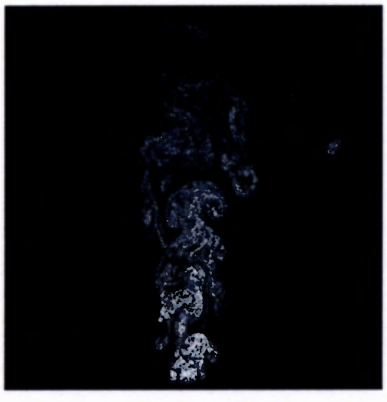

e. 1600 Hz

f. 2000 Hz

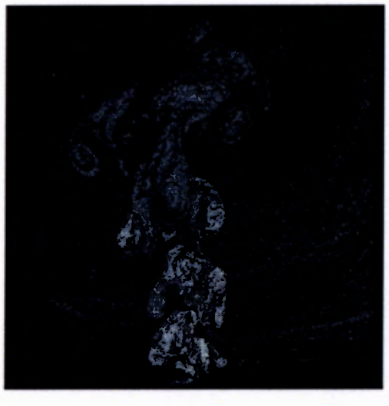

g. 3400 Hz

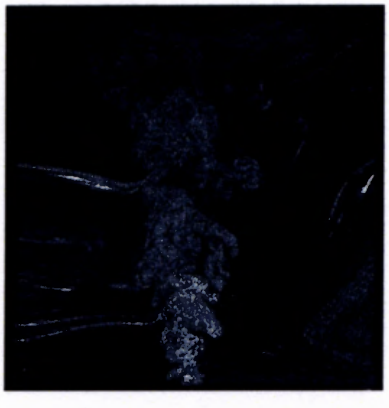

h. 3800 Hz

Figure 2.2 Flow visualizations for varying excitation frequencies.

Figures 2.2a-h show the effects of varying the frequency on the structure of the jet. At the low frequency of 600 Hz (figure 2.2a), a distinct jet can be observed, although it is quite weak and imperceptable to the touch. A series of three vortex rings forms near the orifice. These three rings ultimately break up, with each half of the ring taking its own path to the far right and left of the jet in distinct streaks. The streaks open into a V pattern as they move upwards. Eventually, the streaks come together again and form a larger ring before disappearing from the view.

As the frequency is increased (figure 2.2b), the three vortex rings tend to come together and form a single stream near the centerline of the jet. At a certain distance downstream the jet begins to become unstable and ultimately breaks up. At 800 Hz, the three vortex rings maintain their shape for a longer period. Downstream, they begin to coalesce and ultimately break up. It is at this frequency that the jet is the strongest and exherts the greatest force on particles placed in front of it.

At 1200 Hz (figure 2.2d), the characteristic vortex rings seen in the previous images are no longer present. A mushroom shaped plume is observed very close to the orifice, but quickly breaks up. The jet is fully turbulent without any distinct features in the far field. As the frequency is further increased, the jet appears to come together once again. Distinct mushroom shapes can be observed in alternating patterns rising upwards. The jet also appears to be more cohesive, maintaining its width as it moves downstream and ultimately breaks apart.

A very interesting profile was observed at 2000 Hz. The jet appears as a lump near the orifice. The lump is perfectly balanced, dancing slightly at a frequency corresponding to the excitation frequency of the speaker. The jet was very stable as long

as the frequency was maintained. However, slight shift in frequency quickly caused the lump to break apart.

Between the frequencies of 2000 and 3400 Hz, no jet was observed. As the frequency approached 3400 Hz, a jet once again begins to emerge. A trail of "roll-ups" appears visible in the wide jet. The shape is maintained well downstream of the orifice. Again, between the frequencies of 3400 and 3800 Hz no jet was observed. At the frequency of 3800 Hz, corresponding to a very low actuator displacement, the jet in figure 2.2h became visible. Although the jet appears to resemble that of the jet observed at 1200 Hz, it is much weaker. There is very little momentum transferred to the surrounding fluid by the vibrating speaker, but its effect on the surrounding fluid is still apparent.

2.3 Cooling of Electronics

The surging demand for smaller and faster chips, as found in much of today's electronic packaging, has spurred the need for more effective methods of cooling. Chips are using more power and getting hotter as more transistors are being put in them. Heat is thus becoming more concentrated and harder to dissipate in the cramped quarters. This heat crisis is the origin of a bottleneck in, e.g., increasing processing speed and component reliability.

Traditional cooling techniques use metallic heat sinks to conduct thermal energy away from devices, and then transfer this energy to air which is typically circulated by fans. However, cooling fans have a number of limitations. For instance, much of the circulated air bypasses the heat sinks and does not mix well with the thermal boundary

layer that forms on the fins. Fans placed directly over heat sinks have "dead areas" where their motor assemblies block air flow. Furthermore, as designers boost air flow to increase cooling, fans use more energy, create more audible noise and take up more space.

The use of liquid coolants has been proposed as a possible means of reducing heat build up. However, liquids pose their own set of problems. The piping required to channel the liquid can itself be bulky and cumbersome and complicated to fabricate. Furthermore, there is the risk that the coolant can leak on to the circuitry if the seal fails.

By using a pulsed jet in place of a fan, a jet of air can be generated that can be aimed at a heat source do dissipate heat. These jets are characterized by a buildup of vortex rings near the orifice of the device. Further downstream, the vortices breakup and coalesce into a fully developed turbulent jet. This type of jet flow is very effective in mixing with ambient air and breaking up thermal boundary layers.

In the two figures of Figure 2.3, a synthetic jet is aimed at a plate directly opposite to the exit of the jet at a distance of 7/16 inch. In the upper picture, the jet is operated at low frequency. The two large vortices that are created are exactly balanced under the plate. For cooling applications, this would not be very effective since the built up heat would not be convected outward. However, when the frequency of the jet is increased, the vortices begin to break up and leak outward. This outward momentum carries with it the heat generated by the electronic device.

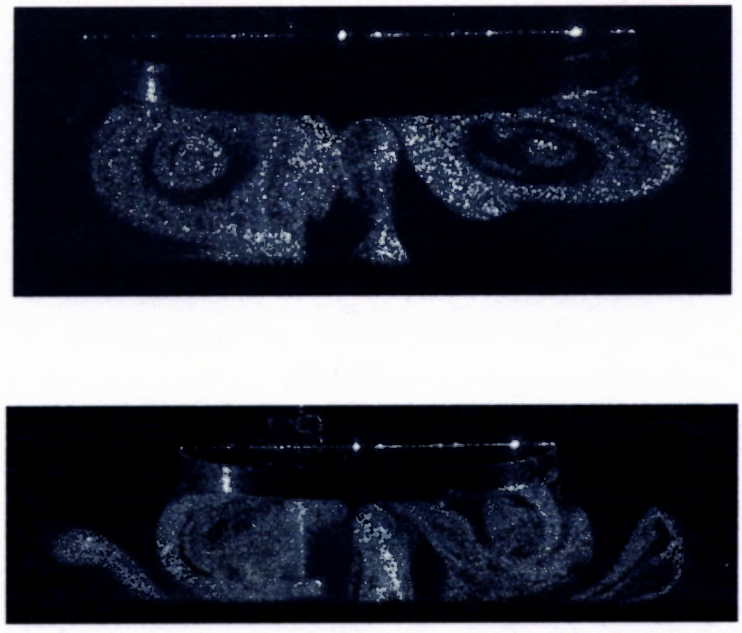

Figure 2.3 Synthetic jet aimed at a wall directly opposite to the jet orifice.

To test the effectiveness of a synthetic jet on cooling, a resistor was mounted to the upper plate and allowed to heat up until it reached an equilibrium temperature of 90 degrees Celsius. The resistor properties are shown in Table 2.1. The jet was then turned on and operated at various frequencies. As can be seen by the measurements shown in Figure 2.4, at an excitation frequency of 450Hz, the jet is quite effective at lowering the resistor's temperature by 15 degrees Celsius.

Table 2.1 Resistor properties.

Diameter	5/16"
Length	1 1/2"
Voltage	11.5 Volts
Resistance	20Ω
Current	66 amps

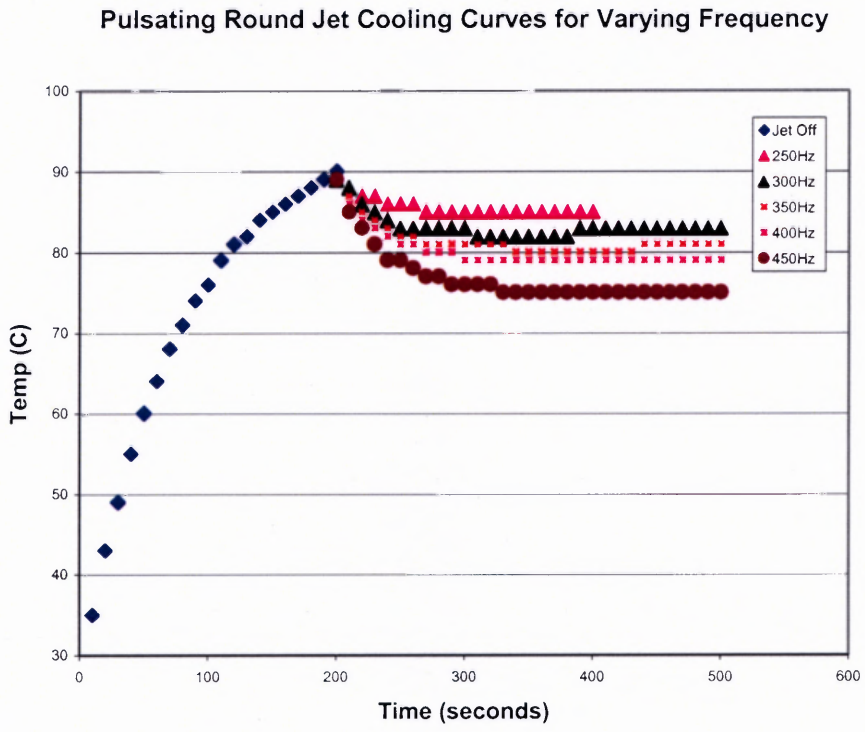

Figure 2.4 Synthetic Jet cooling effectiveness on heated resistor.

Further cooling tests were conducted to compare the effectiveness of the synthetic jet against a more conventional heat sink. The properties of the resistor and the heat sink are shown in

Table **2.2** and Table 2.3, respectively. The results, displayed in Figure 2.5, clearly show that the heat sink lowered the temperature by only 8 degrees, from 100 to 92 degrees Celsius, and that the temperature remained steady after an initial drop. The synthetic jet, on the other hand, lowered the temperature by 16 degrees, down to 84 degrees Celsius. The effectiveness of the synthetic jet by itself to cool electronic circuitry is quite evident. A further advantage is that the synthetic jet is more compact than the heat sink and could be readily incorporated into circuit board.

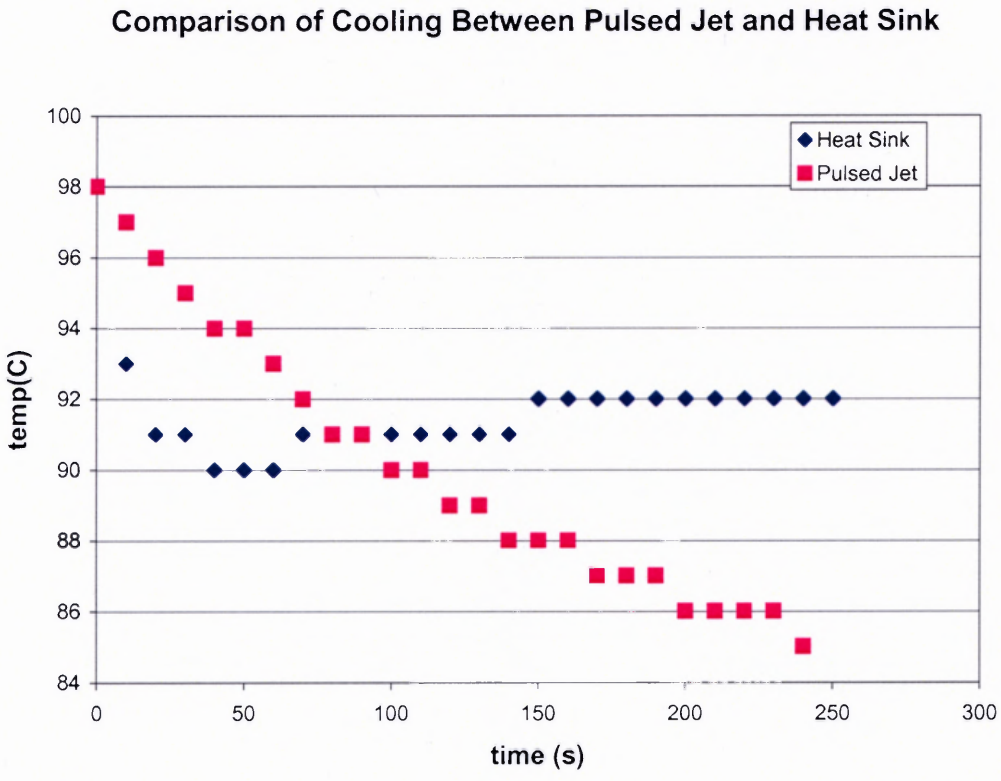

Figure 2.5 Comparison of cooling effectiveness between a synthetic jet and a heat sink.

Table 2.2 Resistor properties.

Diameter	9/16"
Length	1 1/16"
Voltage	11.5 Volts
Resistance	20Ω
Current	66 amps

Table 2.3 Heat sink dimensions.

Height	0.5"
Length	1 3/16"
Width	1 1/16"

CHAPTER 3

MEMBRANE DEFORMATION

3.1 Membrane Mechanics

A clear understanding of the large deflection behavior of thin plates (or membranes) is a crucial design element for many microfabricated devices, such as micropumps and pressure sensors. Similarly, a key component of a synthetic jet is the vibration of a square, rectangular, or circular membrane. Square or rectangular geometries lend themselves well to common wet etching microfabrication techniques, and are, therefore, more common in MEMS devices. To induce separation of the fluid from the membrane, the amplitude of the oscillations must be of sufficient magnitude and frequency. The large amplitude that is required necessitates a nonlinear large deflection analysis to accurately predict the membrane deflection for a given pressure loading. In addition, electrostatic actuation can be readily incorporated into microdevices, and is the preferred method of applying a uniformly distributed load to actuate a membrane. A cross-sectional view of the proposed synthetic jet is shown in Figure 3.1.

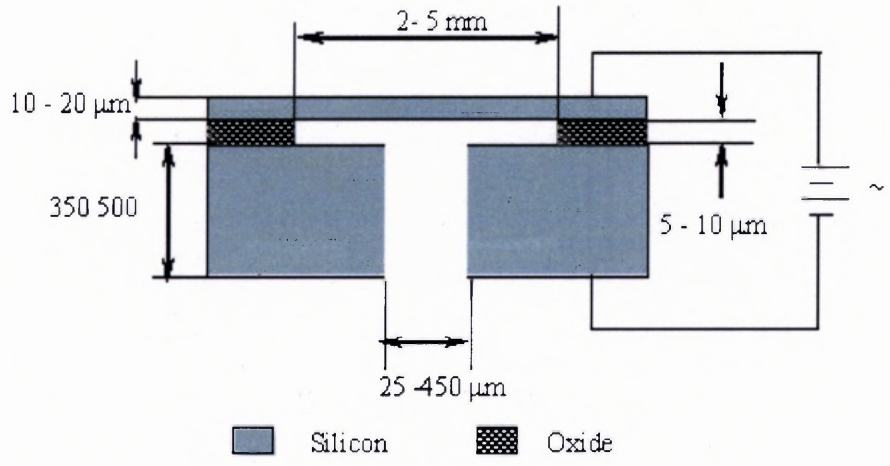

Figure 3.1 Microjet cross section and dimensions.

Solving the coupled, nonlinear, partial differential equations for the large deflections of thin plates is a difficult task at best. Exact solutions of the governing differential equations have been obtained for very few cases only. Consequently, the importance of accurately predicting the large deflection behavior of plates as used in microdevices has resulted in several publications addressing the issue (1,6). However, a ready equation that deals specifically with square and rectangular plates has not been presented in the literature. An analytical solution is desirable not only for its ease of use, but also because it makes it possible to easily vary parameters to gain additional insight to the problem.

Several sources, including Timoshenko and those who refer to Timoshenko, provide an equation for calculating large deflections of thin plates. A problem with such equation, however, is that it defines the deflection for a given value of Poisson's ratio, specifically a Poisson ratio's value of 0.25 (22,24). Presumably, this is done to simplify the development of the equations by eliminating one variable. While the value of 0.25 is

common in many engineering applications and can be applied for a wide range of materials, many newer materials have Poisson values that greatly differ from 0.25. The development is further simplified by assuming that the plate is square, although there are some tables available that can be used for certain rectangular plates based on the aspect ratio of the sides (22,23,24). Ideally, it is desirable to have an equation that is applicable to *any* Poisson ratio and *any* rectangular dimension, and allows the deflection to be quickly and accurately determined. For circular plates, such an equation is readily available (6). Therefore, a key goal of this thesis consists of deriving such an equation for square and, more generally, rectangular plates. A detailed analysis of the membrane deflection for circular membranes is also included.

3.2 Energy Method for Square and Rectangular Plates Subject to Large Deflections

The energy method offers a relatively simple and accurate technique for predicting the deflection of a plate subjected to a uniform load p_0 per unit area, as in Figure 3.2 (19,22,24). When the plate deflection w is equal to or larger than the thickness t ($w \geq t$), the midplane of the plate stretches, developing in-plane tensile stresses that resist the stretching. The small deflection plate theory neglects this effect.

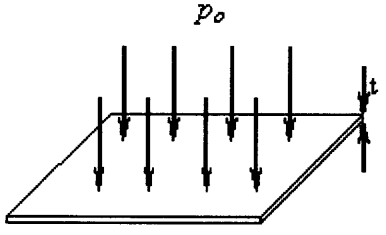

Figure 3.2 Thin plate with a uniformly distributed load.

Using potential theory, the potential energy of a body is given by

$$\Pi = (U_b + U_m) - W \tag{3.1}$$

where Π is the total energy, U_b is the strain energy due to bending, U_m is the strain energy due to the stretching of the midplane, and W is the work done by the distributed load. The potential energy of the body must be at a minimum when the displacements satisfy the boundary and equilibrium conditions. Note that for very thin plates, U_b can be neglected since the deflection is many times larger than the thickness of the plate. The membrane stain energy, U_m, is represented by the following area integral

$$U_m = \frac{Et}{2(1-\upsilon^2)} \iint \left[\varepsilon_x^2 + \varepsilon_y^2 + 2\upsilon\varepsilon_x\varepsilon_y + \frac{1}{2}(1-\upsilon)\gamma_{xy}^2 \right] dxdy \tag{3.2}$$

$$\begin{aligned} \varepsilon_y &= \frac{\partial v}{\partial y} + \frac{1}{2}\left(\frac{\partial w}{\partial y}\right)^2 \\ \varepsilon_x &= \frac{\partial u}{\partial x} + \frac{1}{2}\left(\frac{\partial w}{\partial x}\right)^2 \\ \gamma_{xy} &= \frac{\partial v}{\partial x} + \frac{\partial u}{\partial y} + \frac{\partial w}{\partial x}\frac{\partial w}{\partial y} \end{aligned} \tag{3.3}$$

where ε_x , ε_y , γ_{xy} are the midplane strain-displacement relations due to bending and stretching of the plate, E is the modulus of elasticity, t is the plate thickness and ν is Poisson's ratio.

The work done by the uniformly distributed load is given by

$$W = \iint p_0 w \, dxdy \tag{3.4}$$

where p_o is the uniform load and w is the deflection normal to the plane.

If the origin of the coordinates x, y is located at the center of the plate, as shown in Figure 3.3, the displacements in the x,y, and z directions can be represented by the set of equations (3.5).

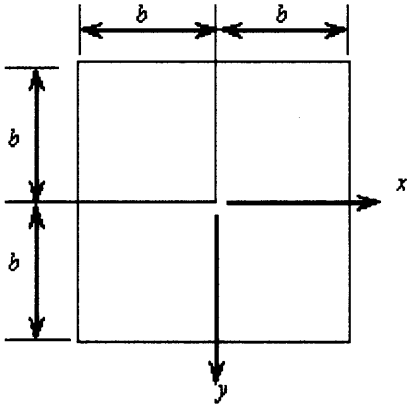

Figure 3.3 Thin plate coordinate alignment.

$$
\begin{aligned}
w &= a_0 \cos\frac{\pi x}{2b}\cos\frac{\pi y}{2b} \\
u &= c_0 \sin\frac{\pi x}{b}\cos\frac{\pi y}{2b} \\
v &= c_0 \sin\frac{\pi y}{b}\cos\frac{\pi x}{2b}
\end{aligned}
\tag{3.5}
$$

For the clamped plate, the boundary conditions that must be satisfied are

$$
w = 0 \quad \text{and} \quad \frac{\partial w}{\partial x} = \frac{\partial w}{\partial y} = 0 \tag{3.6}
$$

The membrane strain energy and work done by the applied load then become

$$U_m = \frac{Et}{2(1-\nu)}\left[\frac{\pi^4 a_0^4}{512b^2}(13-3\nu)+\frac{\pi^2 c_0 a_0^2}{3b}(2\nu-3)+c_0^2\left[\frac{\pi^2}{4}(9-\nu)+\frac{16}{9}(1+\nu)\right]\right] \quad (3.7)$$

$$W = \int_{-b}^{b}\int_{-b}^{b} p_0 a_0 \cos\frac{\pi x}{2b}\cos\frac{\pi y}{2b}\,dxdy = \frac{16}{\pi^2}b^2 p_0 a_0 \quad (3.8)$$

Applying the condition that the potential energy must be minimum to satisfy the boundary and equilibrium conditions makes it possible to solve for the unknown coefficients a_o and c_o. The maximum deflection w_{max} occurs at the center of the plate and can be determined using the first equation in the set of equations (3.6)

$$\frac{\partial \Pi}{\partial a_0} = 0 \quad and \quad \frac{\partial \Pi}{\partial c_0} = 0 \quad (3.9)$$

$$w_{\max} = a_0 = \sqrt[3]{\frac{32b^4 p_0}{\pi^6 Et}\frac{1-\nu^2}{\frac{13-3\nu}{128}-\frac{4(3-2\nu)^2}{9\pi^2(9-\nu)+64(1+\nu)}}} \quad (3.10)$$

$$c_0 = \frac{6\pi^2 a_0^2}{b}\frac{(3-2\nu)}{9\pi^2(9-\nu)+64(1+\nu)} \quad (3.11)$$

Similarly, the coefficients a_o, c_o, and the maximum deflection w_{max} are determined for a rectangular plate. The derivation follows that for a square plate. The coordinates x, y are set up as in the square plate, but the sides are now of length 2a-2b, rather than 2b-2b (Figure 3.4), making the solution algebraically more tedious than in the square case, but

still yielding an analytical result. The expressions for the displacements are also modified to account for the different lengths a and b.

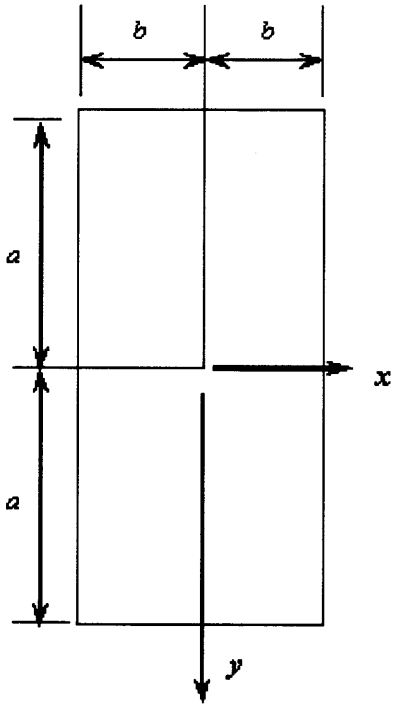

Figure 3.4 Rectangular plate with sides of lengths 2a-2b.

$$
\begin{aligned}
w &= a_0 \cos\frac{\pi x}{2b}\cos\frac{\pi y}{2a} \\
u &= c_0 \sin\frac{\pi x}{b}\cos\frac{\pi y}{2a} \\
v &= c_0 \sin\frac{\pi y}{a}\cos\frac{\pi x}{2b}
\end{aligned}
\tag{3.12}
$$

For a rectangular plate, the membrane strain energy and work done by the applied load are given by

$$U_m = \frac{Et}{2(1-\nu^2)}\left[\frac{\pi^4 a_0^4}{1024a^3b^3}\left[9\left(a^4+b^4\right)+2a^2b^2(4-3\nu)\right]-\right. \tag{3.13}$$

$$\left.\frac{\pi^2 c_0 a_0^2}{6a^2b^2}\left[2(a^3+b^3)+(1-2\nu)(ab^2+a^2b)\right]+c_0^2\left[\frac{\pi^2(9-\nu)}{8ab}(a^2+b^2)+\frac{16}{9}(1+\nu)\right]\right]$$

$$W = \int_a^a \int_b^b p_0 a_0 \cos\frac{\pi x}{2b}\cos\frac{\pi y}{2a}dxdy = \frac{16}{\pi^2}abp_0a_0 \tag{3.14}$$

The resulting solution for the coefficients c_o and a_o reads

$$c_0 = \frac{6\pi^2 a_0^2}{ab}\frac{2(a^3+b^3)+(1-2\nu)(ab^2+a^2b)}{9\pi^2(9-\nu)(a^2+b^2)+128ab(1+\nu)} \tag{3.15}$$

$$a_0 = \sqrt[3]{\frac{32a^4b^4p_0}{Et\pi^6}\frac{1-\nu^2}{\frac{A}{256}-2BC}} \tag{3.16}$$

where the coefficients A, B, and C in the above equations take the form

$$\begin{aligned} A &= 9\left(a^4+b^4\right)+\left(2a^2b^2\right)(4-3\nu) \\ B &= 2\left(a^3+b^3\right)+(1-2\nu)\left(ab^2+a^2b\right) \\ C &= \frac{2\left(a^3+b^3\right)+(1-2\nu)\left(ab^2+a^2b\right)}{9\pi^2(9-\nu)\left(a^2+b^2\right)+128ab(1+\nu)} \end{aligned} \tag{3.17}$$

An expression for determining the maximum deflection as a function of the lengths a-b and the Poisson ratio for the case of a rectangular plate has therefore been obtained. A comparison between the Finite Element Method (FEM) solution using ANSYS and the above analytical expressions is shown in Figure 3.5.

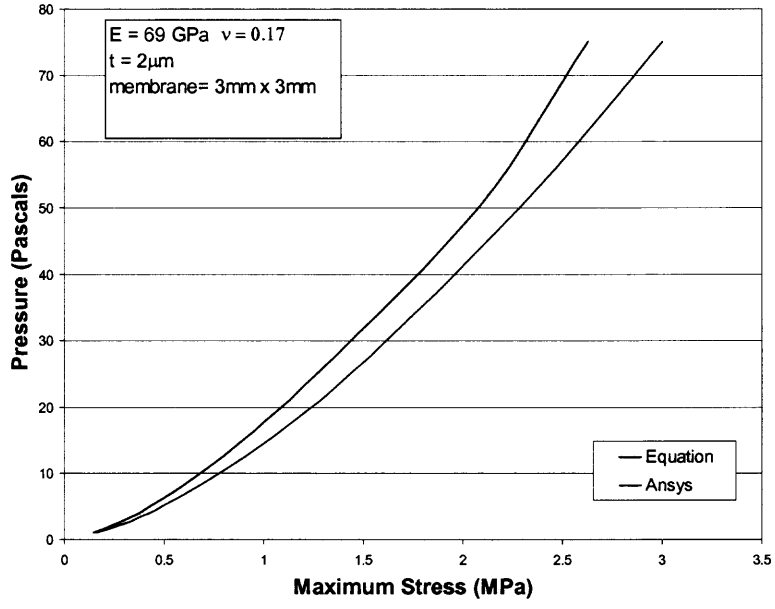

Figure 3.5 Comparison of FEM results using ANSYS and the analytical expression obtained for large displacements of a membrane.

3.3 Stresses in a Rectangular Membrane Subject to Large Deflections

Applying Hooke's law, the stresses in terms of strains are given by

$$\sigma_x = \frac{E}{1-\nu^2}\left(\varepsilon_x + \nu\varepsilon_y\right)$$
$$\sigma_x = \frac{E}{1-\nu^2}\left(\varepsilon_y + \nu\varepsilon_x\right) \tag{3.18}$$

Substituting the set of equations (3.12) into the equations (3.3), the stresses at any point on a rectangular plate are found to take the following expressions

$$\sigma_x = \frac{E}{1-\nu^2}\left[\begin{array}{l}\frac{c_0\pi}{b}\left(\cos\frac{\pi x}{b}\right)\left(\cos\frac{\pi y}{2a}\right)+\frac{a_0{}^2\pi^2}{8b^2}\left(\sin\frac{\pi x}{2b}\right)^2\left(\cos\frac{\pi y}{2a}\right)^2+ \\ \nu\left[\frac{c_0\pi}{a}\left(\cos\frac{\pi y}{a}\right)\left(\cos\frac{\pi x}{2b}\right)+\frac{a_0{}^2\pi^2}{8a^2}\left(\cos\frac{\pi x}{2b}\right)^2\left(\sin\frac{\pi y}{2a}\right)^2\right]\end{array}\right] \tag{3.19}$$

$$\sigma_y = \frac{E}{1-\nu^2}\left[\begin{array}{l}\frac{c_0\pi}{a}\left(\cos\frac{\pi y}{a}\right)\left(\cos\frac{\pi x}{2b}\right)+\frac{a_0{}^2\pi^2}{8a^2}\left(\sin\frac{\pi y}{2a}\right)^2\left(\cos\frac{\pi x}{2b}\right)^2+ \\ \nu\left[\frac{c_0\pi}{b}\left(\cos\frac{\pi x}{b}\right)\left(\cos\frac{\pi y}{2a}\right)+\frac{a_0{}^2\pi^2}{8b^2}\left(\cos\frac{\pi y}{2a}\right)^2\left(\sin\frac{\pi x}{2b}\right)^2\right]\end{array}\right] \tag{3.20}$$

In the center, where $x = y = 0$, the above equations simplify to

$$\sigma_{x(x=0,y=0)} = \frac{Ec_0}{1-\nu^2}\left(\frac{1}{b}+\nu\frac{1}{a}\right) \tag{3.21}$$

$$\sigma_{y(x=0,y=0)} = \frac{Ec_0\pi}{1-\nu^2}\left(\frac{1}{a}+\nu\frac{1}{b}\right) \tag{3.22}$$

For a square plate for which $a = b$ the above formula reduce further to

$$\sigma_{x(x=0,y=0)} = \sigma_{y(x=0,y=0)} = \frac{Ec_0\pi}{b(1-\nu)} \tag{3.23}$$

The maximum stresses are thus found at the middle point of the long side of the plate. Using the system of coordinates defined in Figure 3.4, it follows that these maximum stresses at the location $x = 0, y = a$ take the form

$$\sigma_{x(x=0,y=a)} = \frac{E\nu}{1-\nu^2}\left(\frac{a_0^2\pi^2}{8a^2} - \frac{c_0\pi}{a}\right) \tag{3.24}$$

$$\sigma_{y(x=0,y=a)} = \frac{E}{1-\nu^2}\left(\frac{a_0^2\pi^2}{8a^2} - \frac{c_0\pi}{a}\right) \tag{3.25}$$

Similarly, at the location $x = b, y = 0$ the stresses become

$$\sigma_{x(x=b,y=0)} = \frac{E}{1-\nu^2}\left(\frac{a_0^2\pi^2}{8b^2} - \frac{c_0\pi}{b}\right) \tag{3.26}$$

$$\sigma_{y(x=b,y=0)} = \frac{E\nu}{1-\nu^2}\left(\frac{a_0^2\pi^2}{8b^2} - \frac{c_0\pi}{b}\right) \tag{3.27}$$

While the maximum stress can be predicted to be at the centers of the sides, in practice the maximum stress is often found near the corners, where large concentration factors can result due to corner effects. A way to reduce these high stress values due to corner effects is to slightly round the sharp edges if the fabrication process allows it.

3.4 Energy Method for Circular Membranes Subject to Large Deflection

The above analysis for the displacements and stresses of a square and a rectangular plate is further applied to a circular membrane. The deflection in the z-direction for a circular membrane can be given by (24)

$$w = w_{\max}\left(1-\frac{r^2}{a^2}\right)^2 \tag{3.28}$$

subjected to the boundary condition for a clamped membrane

$$w = 0 \quad \text{and} \quad \frac{\partial w}{\partial r} = 0 \quad \text{at} \quad r = a \tag{3.29}$$

The radial displacement is represented by the following series

$$u = r(a-r)\left(c_1 + c_2 r + c_3 r^2 + ...\right) \tag{3.30}$$

which satisfies the zero displacement boundary condition:

$$u = 0 \quad \text{at} \quad r = 0, r = a \tag{3.31}$$

Taking the first two terms in the series reduces the above to

$$u = r(a-r)(c_1 + c_2 r) \tag{3.32}$$

The midplane strain-displacement relations due to the bending and stretching of the plate are given by

$$\varepsilon_r = \frac{du}{dr} + \frac{1}{2}\left(\frac{\partial w}{\partial r}\right)^2 \tag{3.33}$$

$$\varepsilon_\theta = \frac{u}{r} \tag{3.34}$$

while the strain energy due to bending and stretching takes the expression

$$U_b = \frac{32\pi}{3}\frac{w_{\max}^2}{a^2}D \tag{3.35}$$

$$U_m = \frac{\pi E t}{1-\nu^2}\int_0^a \left(\varepsilon_r^2 + \varepsilon_\theta^2 + 2\nu\varepsilon_r\varepsilon_\theta\right) r\partial r \tag{3.36}$$

The unknowns c_1 and c_2 are found by using the fact that the derivative of the strain energy must vanish, i.e.

$$\frac{\partial U_m}{\partial c_1} = 0 \quad \text{and} \quad \frac{\partial U_m}{\partial c_2} = 0 \tag{3.37}$$

The two unknown coefficients are then found to be

$$c_1 = -\frac{{w_{\max}}^2}{a^3}\frac{(89\nu - 179)}{126} \tag{3.38}$$

$$c_2 = \frac{{w_{\max}}^2}{a^4}\frac{(13\nu - 79)}{42} \tag{3.39}$$

The work done by the uniformly distributed load reads

$$W = 2\pi \int_0^a w p_0 r dr = 2\pi\, p_0 w_{\max} \int_0^a \left(1 - \frac{r^2}{a^2}\right) r dr \tag{3.40}$$

Applying the energy method, $\Pi = U_{(b+m)} - W$ and $\frac{\partial \Pi}{\partial w_{\max}} = 0$, the maximum displacement is obtained in dimensionelss form

$$\frac{pa^4}{Et^4} = \frac{2.27 + 1.28\nu - 0.84\nu^2}{1-\nu^2}\left(\frac{w_{\max}}{t}\right)^3 + \frac{5.33}{1-\nu^2}\frac{w_{\max}}{t} \tag{3.41}$$

It is noted that for small displacements, the first term on the right hand side of the above equation does not contribute significantly but this contribution becomes important for

large deflections. In this latter case, the linear term on the right hand side is less significant compared to the first term on the same side.

3.5 Stresses in a Circular Membrane Subject to Large Deflections

The maximum bending stresses are given by

$$\sigma_b = \frac{6M}{t^2} \tag{3.42}$$

In the radial and theta direction the maximum bending stresses become

$$\sigma_r = \frac{3pz}{4t^3}\left[(1+\nu)a^2 - (3+\nu)r^2\right] \tag{3.43}$$

$$\sigma_\theta = \frac{3pz}{4t^3}\left[(1+\nu)a^2 - (1+3\nu)r^2\right] \tag{3.44}$$

where z is taken at the midplane, $z = t/2$.

The bending stress takes the following expressions at the edge, $r = a$,

$$\frac{\sigma_{b(r=a)}a^2}{Et^2} = \frac{3}{4}\left[\left(\frac{2.27+1.28\nu-0.84\nu^2}{1-\nu^2}\right)\left(\frac{w_{\max}}{t}\right)^3 + \frac{5.33}{1-\nu^2}\frac{w_{\max}}{t}\right] \tag{3.45}$$

and at center, $r = 0$,

$$\frac{\sigma_{b(r=0)}a^2}{Et^2} = \frac{3}{8}\left[\frac{1+\nu}{1-\nu^2}\left(2.27+1.28\nu-0.84\nu^2\right)\left(\frac{w_{\max}}{t}\right)^3 + 5.33\frac{1+\nu}{1-\nu^2}\frac{w_{\max}}{t}\right] \tag{3.46}$$

The membrane stress is given by

$$\sigma_m = \frac{N_r}{h} = \frac{1}{h}\frac{Eh}{1-\nu^2}\left(\varepsilon_r + \nu\varepsilon_\theta\right) \tag{3.47}$$

At the edge, $r = a$, it reduces to

$$\frac{\sigma_{m(r=a)}a^2}{Et^2} = \frac{106+50\nu}{126\left(1-\nu^2\right)}\left(\frac{w_{\max}}{t}\right)^2 \tag{3.48}$$

while at the center, $r = 0$, it takes the form

$$\frac{\sigma_{m(r=0)}a^2}{Et^2} = \frac{1+\nu}{1-\nu^2}\frac{179-89\nu}{126}\left(\frac{w_{\max}}{t}\right)^2 \tag{3.49}$$

Finally, the total stress is the sum of the bending and membrane stresses,

$$\sigma_t = \sigma_b + \sigma_m \tag{3.50}$$

The stresses are depicted graphically in Figure 3.6. For the example, a Poisson ratio of $\nu = 0.1$ is used. It can be seen from the graph that the highest stresses are the bending stresses at the edge.

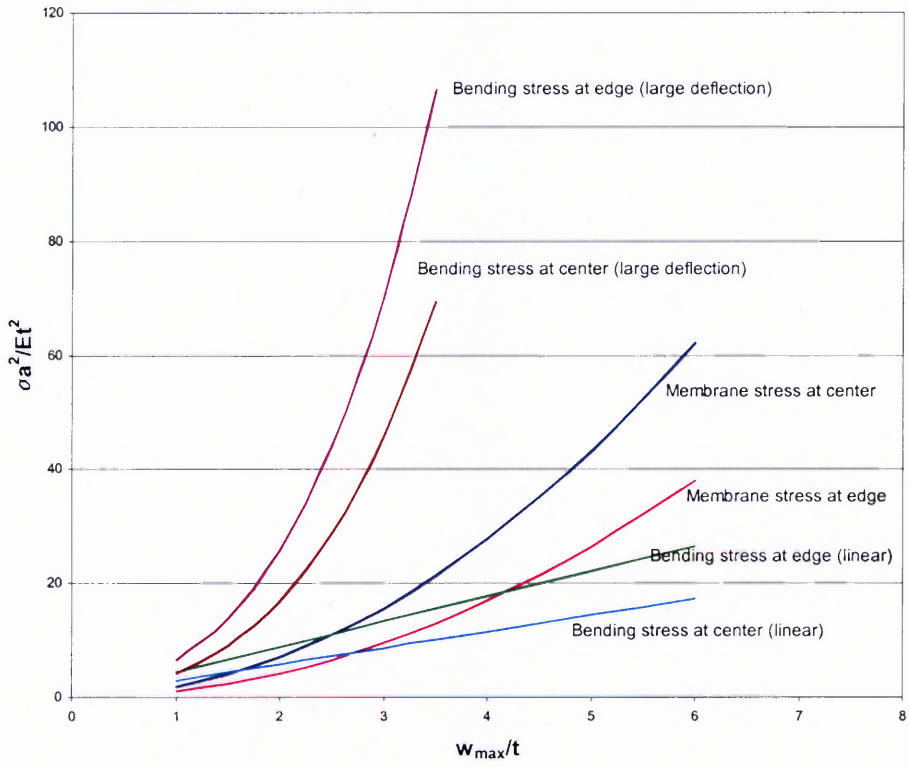

Figure 3.6 Stresses for a clamped circular plate subjected to a large deflection, for a Poisson's ratio of $\nu = 0.1$.

In Figure 3.7, the displacements of a square and a round membrane are compared graphically. The square line markers denote the nondimensionalized displacement relations for a square plate while the round line markers depict that of a circular plate. It is interesting to note that an equivalent pressure results in a larger maximum displacement for a square membrane. Furthermore, the larger surface area of a square membrane leads to a larger volume displacement when the membrane is deflected. For the above reasons, a square membrane is the preferred geometry. However, one needs to

keep in mind that, in practice, high concentration factors can be present near the corners of a square membrane which can lead to fractures in the membrane.

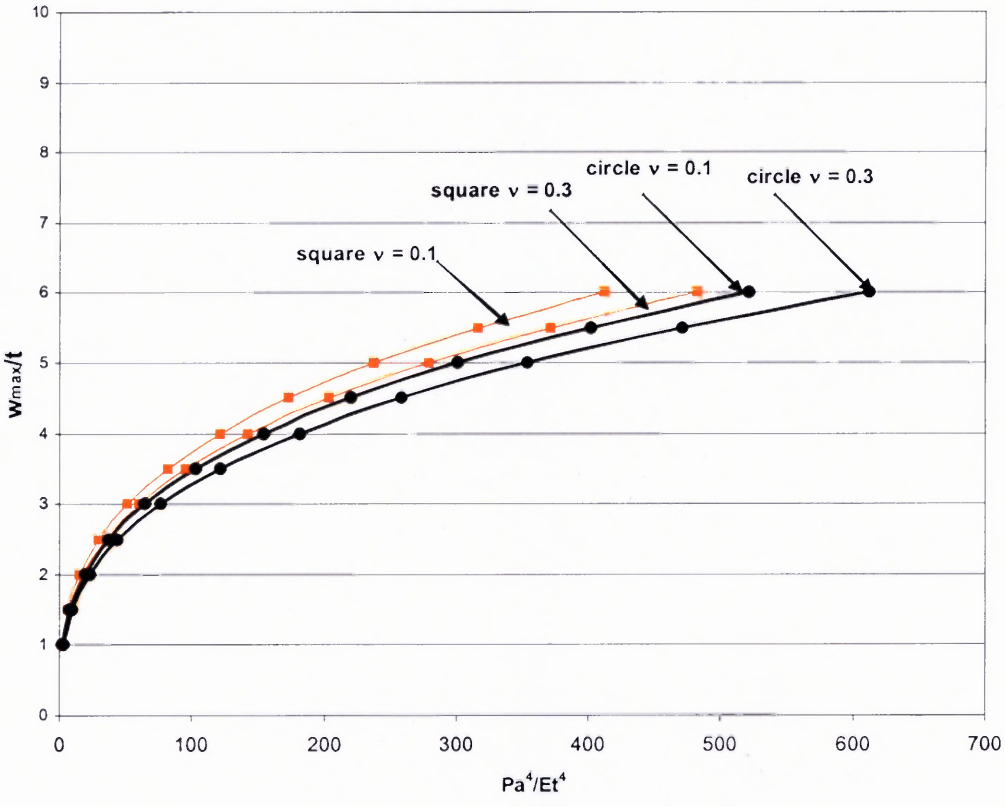

Figure 3.7 Comparison of pressure versus deflection for thin circular and square plates with a large deflection.

3.6 Natural Frequency and Dynamic Deflection

A critical parameter, when considering a vibrating plate, is its resonant frequency. The largest displacements and most efficient transfer of energy will occur when the plate is excited close to its natural frequency. The first mode of vibration, characterised by the largest deflection, is shown in Figure 3.8 for a rectangular plate.

The plate deflection during vibration is given by

$$w = w_0 \cos \omega_n t \tag{3.51}$$

where ω_n is the natural circular frequency, and w_0 is a function of x and y that determines the mode of vibration. Referring to the set of equations (3.5), the deflection w, which satisfies the boundary conditions and closely approximates the shape of the first mode, is assumed for w_0 to be

$$w_0 = a_0 \cos\frac{\pi x}{2b} \cos\frac{\pi y}{2b} \tag{3.52}$$

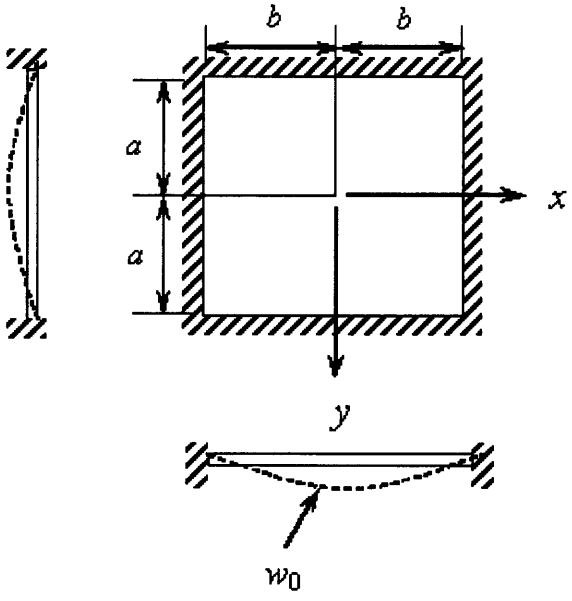

Figure 3.8 Fundamental mode of a square membrane.

The energy method is applied once more to determine the plate's natural frequency. The kinetic energy must be added to the total energy (3.1). The kinetic energy is expressed by

$$T_{\max} = \frac{\overline{m}}{2} \iint \dot{w}^2 dxdy \tag{3.53}$$

which can be rewritten as

$$T_{\max} = \frac{\overline{m}}{2} w_n^2 \iint w_0^2 dxdy \tag{3.54}$$

or

$$T_{\max} = \frac{\overline{m}}{2} \omega_n^2 \int_{-a}^{a} \int_{-b}^{b} \left(a_0 \cos\frac{\pi x}{2b} \cos\frac{\pi y}{2b} \right)^2 dxdy \tag{3.55}$$

where $\overline{m}$, the mass per unit area, is defined as

$$\overline{m} = \rho t \tag{3.56}$$

Upon integrating, the following solution is obtained for the maximum potential and kinetic energies

$$U_m = \frac{Et}{2(1-\nu^2)} \left[\frac{\pi^4 a_0^4}{512 b^2} (13 - 3\nu) + \frac{\pi^2 c_0 a_0^2}{3b} (2\nu - 3) + c_0^2 \left[\frac{\pi^2}{4} (9 - \nu) + \frac{16}{9} (1 + \nu) \right] \right] \tag{3.57}$$

$$T = \frac{\omega_n^2 \overline{m}}{2} b^2 a_0{}^2 \tag{3.58}$$

To determine the natural circular frequency, the total potential energy

$$\Pi = U_m - T \tag{3.59}$$

is made minimum, i.e.

$$\frac{\partial \Pi}{\partial a_0} = 0 \text{ and } \frac{\partial \Pi}{\partial c_0} = 0 \tag{3.60}$$

The unknowns a_0 and c_0 were determined previously (equations (3.10) and (3.11)). The resonant frequency of the lowest mode of vibration for a square plate subjected to a large displacement can now be obtained

$$\omega_n = \left[\frac{\pi^4 a_0^2}{2b^4} \frac{Et}{\bar{m}(1-\nu^2)} \left(\frac{13-3\nu}{128} - \frac{4(3-2\nu)^2}{9\pi^2(9-\nu)+64(1+\nu)} \right) \right]^{1/2} \tag{3.61}$$

For a rectangular plate, the solution is found in the same manner, but is algebraically more tedious to derive due to the geometric variables a and b, the plate width and height. The frequency of the lowest mode of vibration for a rectangular plate is then found to take the form

$$\omega_n = \left[\frac{\pi^4 a_0^2}{2a^4 b^4} \frac{Et}{\bar{m}(1-\nu^2)} \left(\frac{3}{1024} A - 2BC \right) \right]^{1/2} \tag{3.62}$$

where A, B, and C are

$$\begin{aligned} A &= 9\left(a^4 + b^4\right) + 2a^2b^2\left(4-3\nu\right) \\ B &= 2\left(a^3 + b^3\right) + \left(1-2\nu\right)\left(ab^2 + a^2b\right) \\ C &= \frac{2(a^3+b^3)+(1-2\nu)(ab^2+a^2b)}{9\pi^2(9-\nu)(a^2+b^2)+128ab(1+\nu)} \end{aligned} \tag{3.63}$$

For small amplitude oscillations, however, bending effects are predominant, and the resonant frequency reads

$$\omega_{n_{\text{bending}}} = 4\left[\frac{1}{6}\left(\frac{1}{a^4} + \frac{256}{441a^2b^2} + \frac{1}{b^4} \right) \frac{Eh^3}{\bar{m}\left(1-\nu^2\right)} \right]^{1/2} \tag{3.64}$$

The total resonant frequency is thus a combination of the resonant frequency for large and small amplitude oscillations, accounting for both membrane and bending effects. Equations (16) and (17) clearly show that, for small amplitudes, the bending resonant frequency is a function of geometry and material properties only, and is not amplitude dependent. For large amplitudes, however, the resonant frequency varies linearly with amplitude. The total resonant frequency is expressed as

$$\omega_n = \sqrt{\omega_{n_{membrane}}^2 + \omega_{n_{bending}}^2} \tag{3.65}$$

The large displacement of the membrane results in an increase in resistance to deflection by the membrane. The stiffening causes a shift in the resonant frequency of the membrane. This effect can be used to "tune" the device to a particular desired resonant frequency. In Figure 3.9 this effect is depicted graphically, where the resonant frequency is plotted against the ratio of the maximum center deflection to the thickness of the membrane. The resonant frequency is constant for an amplitude-to-deflection ratio of approximately 0.5, above which the nonlinearities manifest themselves.

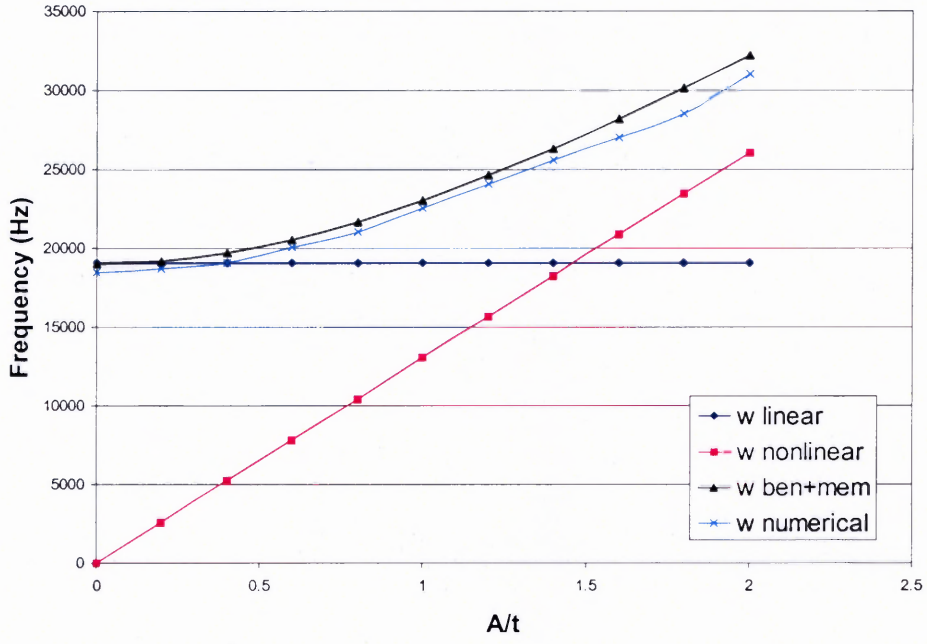

Figure 3.9 Natural frequency for large amplitude deflections of a square membrane.

The natural frequency of the plate in Hertz is deduced by dividing by 2π

$$f_n = \frac{\omega_n}{2\pi} \tag{3.66}$$

Now that the natural frequency is known, the transmissibility, or ratio of maximum dynamic to static displacement, can also be obtained

$$\varepsilon = \frac{1}{1-\left(f/f_n\right)^2} \tag{3.67}$$

where f is the frequency of a simple harmonic disturbance corresponding to the input frequency. As the f/f_n ratio approaches unity, the amplitude of the forced motion becomes infinitely large and resonance occurs. This condition should be avoided, as the

structure could destruct itself. In reality, there is always some damping present in the membrane itself that will keep this from happening. Finally, the dynamic load per unit area is obtained as

$$p_d = \overline{m} g_{in} \varepsilon \tag{3.68}$$

where g_{in} is the input acceleration. The maximum dynamic deflection is found by replacing p_o with p_d in the expression of w_{max}.

CHAPTER 4

ELECTROSTATIC ANALYSIS

4.1 Electrostatic Actuation

In this work, the flexible membrane is displaced electrostatically. Electrostatic actuation offers several advantages over other actuation methods, such as piezo-electric excitation. Most importantly, electrostatic actuation makes it possible to excite the membrane at its fundamental mode at frequencies outside the natural frequency of the membrane. Electrostatic actuation also offers high reliability, very fast response time, low power requirements, and is easily incorporated into micromachined designs.

4.2 The Parallel Plate Capacitor

The equations that describe a basic electrostatic actuator can be readily derived, and can be found in many textbooks (i.e. 19). Therefore, their derivation is not presented here. However, a brief overview is provided for reference. A parallel-plate capacitor in which one plate is allowed to move is considered (Figure 4.1). The plates are separated by a gap g, have a plate area A, and opposite charges $\pm Q$, respectively, when energized. Because the two plates have opposite charges, there is a force of attraction between the two plates.

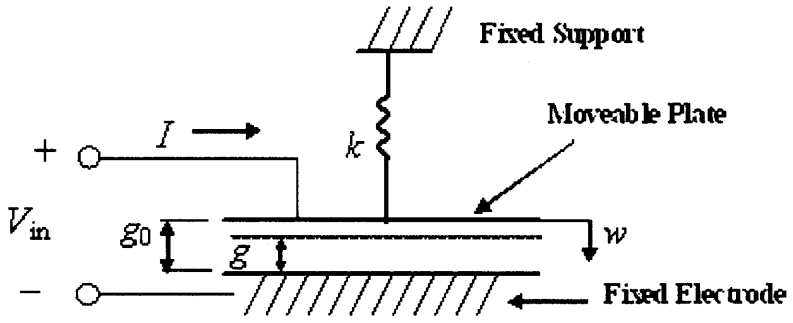

Figure 4.1 Parallel plate capacitor.

When energized, the top plate moves towards the fixed electrode by a distance *w*. A spring force is attached to the top plate to model the restorative force. The voltage determines the force, which stretches the spring, thus determining the change in gap. For two parallel plates, the voltage is related to the force of attraction through the expression

$$F = \frac{\varepsilon A V^2_{in}}{2g^2} \tag{4.1}$$

The gap, g, between the fixed electrode and the flat moveable electrode is $g = g_0 - w$, while the spring force is

$$k = \frac{F}{w} \text{ and } g = g_0 - \frac{\varepsilon A V^2}{kg^2} \tag{4.2}$$

where F is the force, ε is the permittivity of the material in the gap such as air (Farads/meter), A is the area, Vin is the applied voltage, g is the gap, g0 is the gap corresponding to the rest position (zero spring force on zero capacitor charge), and w is the displacement of the end of the spring.

An important behavior that occurs in all electrostatic devices is pull-in. At some critical gap, the system becomes unstable. When this takes place, the control of the moveable plate is lost and the plate collapses against the fixed electrode. This instability occurs when the restorative force in the spring can no longer overcome the force of attraction. The stability criterion dictates that k be

$$k = \frac{\varepsilon A V^2}{g^3} \tag{4.3}$$

which corresponds to a displacement of the top plate equal to

$$w_{pi} = \frac{1}{3} g_0 \tag{4.4}$$

The corresponding voltage required for pull-in to occur is thus

$$V_{pi} = \sqrt{\frac{8kg_0^{\,3}}{27\varepsilon A}} \tag{4.5}$$

4.3 Membrane Capacitor Subject to Small Deflections

If the gap, g, is small and the overall deflection of the membrane is also small (i.e. much smaller than the thickness of the membrane), the membrane actuator can essentially be modeled as a parallel plate capacitor, and the previous analysis holds. Pull-in can still be expected to occur when the membrane deflection is 1/3 of the initial gap.

However, if there is a sufficiently large gap so that the membrane can deform to about the thickness of the membrane itself, fringing effects of the electric field must be considered. However, for membranes undergoing both small and large deformations,

special care needs to be taken. The work of Bao et al. (2) is one example in which a Lagrangian approach was used to solve the problem. Presented here is a closed form analytical solution to this problem.

The deflection of the plate is a function of x and y, and the plate deforms like a membrane undergoing linear deformation.

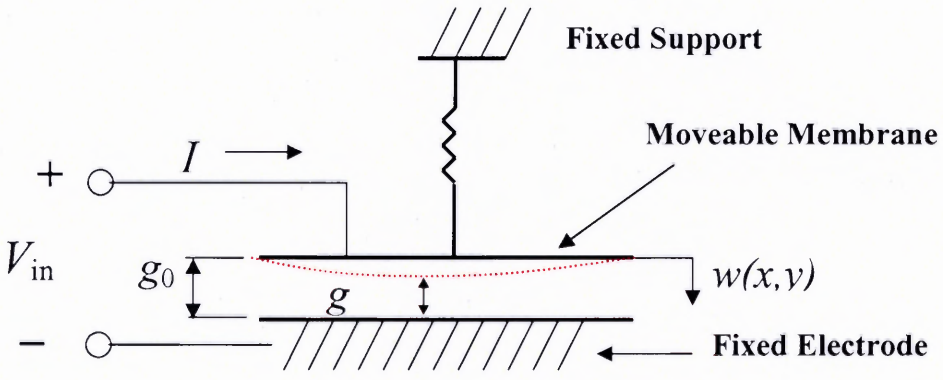

Figure 4.2 Membrane actuator with *w(x,y)*.

The fringing effects are accounted for by developing a pressure for the curved plate that is equivalent to that for a flat plate. This eliminates the gap's dependency on x and y. Working from equation (4.1), the following equivalent pressure is obtained

$$P_{eq} = \frac{\varepsilon V^2}{2g_{eq}^2} \tag{4.6}$$

The equivalent gap being defined by $g_{eq} = g_0 - w_{eq}$, the equivalent pressure can be rewritten as

$$P_{eq} = \frac{\varepsilon V^2}{2} \iint \frac{dxdy}{\left(g_0 - w(x,y)\right)^2} = \frac{\varepsilon V^2}{2} \frac{1}{\left(g_0 - w_{eq}\right)^2} \tag{4.7}$$

Using equation (4.7) to solve for $1/g_{eq}^2$, one obtains

$$\frac{1}{\left(g_0 - w_{eq}\right)^2} = \frac{1}{g_{eq}^{\ 2}} = \iint \frac{dxdy}{\left(g_0 - w(x,y)\right)^2} \tag{4.8}$$

After substituting Equation (4.8) back into equation (4.6) and using

$$w(x,y) = a_m \cos\frac{\pi x}{2a}\cos\frac{\pi y}{2b}$$

where a_m is the maximum center deflection, one obtains the equivalent electrostatic pressure

$$P_{eq} = \frac{\varepsilon V_{in}^2}{2g_0^2} \iint \frac{dxdy}{\left(1 - \bar{a}\cos\frac{\pi x}{2a}\cos\frac{\pi y}{2b}\right)^2} \tag{4.9}$$

Where $\bar{a}$, the normalized membrane maximum center deflection, is equal to $\bar{a} = a_m / g_o$. The integral is solved numerically for values such that $0 \le \bar{a} \le 1$. The integral solution is plotted in

Figure 4.3, and the line is approximated by the function

$$f(x) = x^{-.846} \tag{4.10}$$

where

$$x = (1 - \bar{a}) \tag{4.11}$$

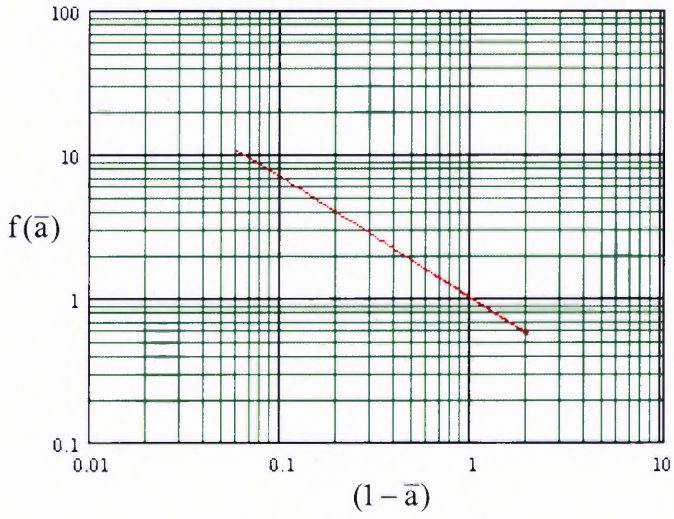

Figure 4.3 Integral solution.

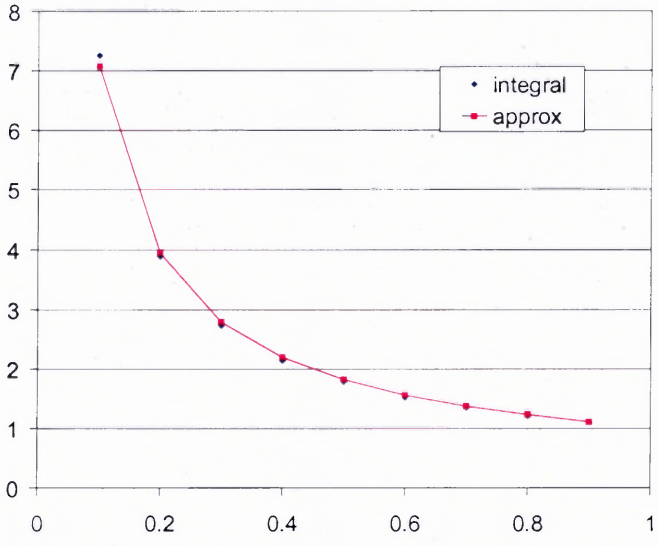

Figure 4.4 Comparison of the integral solution and the curve fitting approximation.

Substituting equation (4.10) for the integral in Equation (4.9) leads to

$$P_{eq} = \frac{\varepsilon V_{in}^2}{2g_0^2} \frac{1}{(1-\bar{a})^{.846}} \tag{4.12}$$

For small deflections, the maximum center displacement is given by

$$a_m = 0.00126 \frac{p_{eq} b^4}{D} \tag{4.13}$$

where D, the flexural rigidity, reads

$$D = \frac{Et^3}{12(1-\nu^2)} \tag{4.14}$$

Equation (4.12) can be solved for p_{eq} and equated to equation (4.13). The voltage required for a desired deflection can then be obtained

$$V_{in}^2 = \frac{2Dg_0^3}{0.00126 b^4 \varepsilon} f(\bar{a}) \tag{4.15}$$

where

$$f(\bar{a}) = \bar{a}(1-\bar{a})^{.846} \tag{4.16}$$

The function given by equation (4.16) has a fixed point, x*, at $\bar{a} = 0.542$, whose stability is determined using

$$(\delta - x^*) f(\delta) \tag{4.17}$$

All points $\delta > 0.542$ result in an unstable solution. Therefore, the maximum center deflection before pull-in occurs is such that

$$a_m = 0.542 g_0 \tag{4.18}$$

The stability plot is given in Figure 4.5.

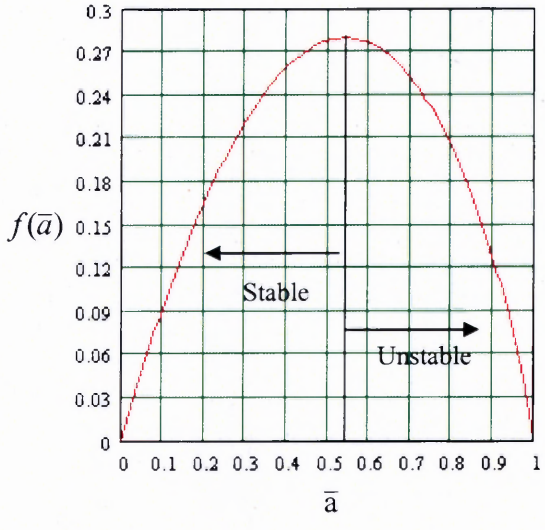

Figure 4.5 Stability plot of normalized membrane deflection for small deflections.

The voltage at which pull-in occurs, V_{pi}, can then be readily obtained by substituting $\bar{a} = 0.542$.

4.4 Membrane Capacitor Subject to Large Deflections

The solution for large deflections follows that for a membrane subject to small deflections. For a square membrane, equation (4.13) is replaced with

$$P_e = \frac{a_m^3 \pi^6 Et}{32b^4 f(\nu)} \tag{4.19}$$

where

$$f(\nu) = \frac{1-\nu^2}{\frac{13-3\nu}{128} - \frac{4(3-2\nu)^2}{9\pi^2(9-\nu)+64(1+\nu)}} \tag{4.20}$$

Equating equation (4.19) to (4.12) gives the maximum center displacement for an input voltage for large amplitude deflections

$$V_{in}^2 = \frac{\pi^6 Etg_0^5}{16b^4 \varepsilon f(\nu)} \bar{a}^3 (1-\bar{a})^{.846} \tag{4.21}$$

In this case, the fixed point occurs at $\bar{a} = 0.780$, and the maximum center deflection before pull-in occurs is

$$a_m = 0.780 g_0 \tag{4.22}$$

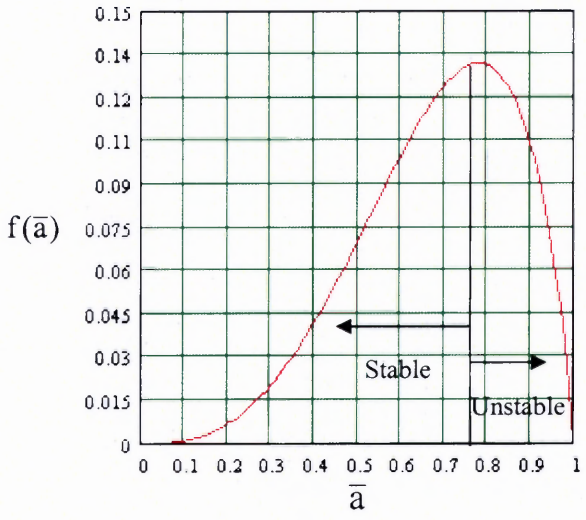

Figure 4.6 Stability plot of normalized membrane deflection for large deflections.

Comparing the pull-in gap for small and large deflections, a substantial increase in the membrane travel results when the membrane is subjected to large deformations. From a control standpoint, this makes the actuator effective over a larger range. On the other hand, the necessary voltage has also increased. This is partially offset in that the voltage has a weaker dependency on the function $f(\bar{a})$.

4.5 Power

The charge on a capacitor is proportional to the voltage across it, as defined by

$$q = CV \tag{4.23}$$

where q is the charge (in coulombs) and V is the voltage (in volts). The ratio of charge to voltage, C, is the capacitance which has units of coulombs per volt or Farads. The capacitance is

$$C = \frac{\varepsilon A}{g} \tag{4.24}$$

As with equation (4.9) the gap, g, is replaced with an equivalent gap, g_{eq}. Therefore, for a membrane capacitor, the capacitance is given by

$$C = \frac{\varepsilon A}{g_0} \iint \frac{dxdy}{\left(1 - \bar{a}\cos\frac{\pi x}{2a}\cos\frac{\pi y}{2b}\right)^2} \tag{4.25}$$

The time rate of change of charge is the current, that is

$$i(t) = \frac{dq(t)}{dt} \tag{4.26}$$

Therefore,

$$i(t) = \frac{dq(t)}{dt} = C\frac{dv(t)}{dt} \tag{4.27}$$

The power delivered to the capacitor is

$$p(t) = v(t)\, i(t) \tag{4.28}$$

Using equation (4.27), this can be rewritten as

$$p(t) = C\,v(t)\frac{dv(t)}{dt} \tag{4.29}$$

Finally, the energy stored in the capacitor is derived from the power delivered to it

$$W_c = \int p(t)dt \tag{4.30}$$

$$W_c = \frac{1}{2}Cv^2(t) \text{ Joules} \tag{4.31}$$

CHAPTER 5

FLUID FLOW ANALYSIS

5.1 Acoustic Analysis

A rigid container having an opening (channel or neck) with a volume of fluid inside is called a Helmholtz resonator. The fluid inside oscillates in the neck in response to the pressure fluctuations generated by the membrane. The assumptions for the Helmholtz resonator are:

(a) The walls of the cavity are rigid

(b) The natural frequency of the resonator is much less than the time required for sound to go through the resonator cavity, allowing the cavity to be modeled as a one-dimensional spring.

(c) The channel is much smaller in cross section than the cavity, so that the fluid velocity in the channel is much larger compared to the fluid velocity in the cavity. Therefore, the fluid in the channel can be modeled as a mass.

The resonator's resonant frequency is given by

$$f = \frac{c}{2\pi}\sqrt{\frac{A}{VL_E}} \tag{5.1}$$

where A is the cross sectional area of the opening, V is the cavity volume, and L_E is the effective length of the neck. For a rectangular cross sectional channel, the effective length is

$$L_E = L_T + \frac{(\pi A_T)^{1/2}}{4} \tag{5.2}$$

where A_T is the channel cross sectional area. From equation (5.1), it is obvious that a larger cavity volume results in lower resonant frequencies. This is due to the fact that for a larger cavity more air must move out of the cavity to relieve a given excess of pressure. Similarly, an increase in neck length also reduces the resonant frequency since there is more resistance to the air entering and exiting the cavity. A larger neck area results in a higher resonant frequency since the air can rush in and out faster. The effects of geometry on the resonance frequency of Helmholtz resonators is addressed in Chanaud (4) and also in Ingard (10).

Smith and Glezer (20) observed peak performance when their piezoelectric driven synthetic jet (not of MEMS scale) was operated at the plate's resonant frequency. This could be expected, as the largest volume displacements in the cavity occur when the oscillating plate in the cavity is driven at resonance. On the other hand, Muller et al. (13,14,15) noted that the peak velocity occurred at some value between the resonant frequency of the membrane and the acoustic resonant frequency of their micro actuator. This indicates that their device was not quite following the valid assumptions for an acoustic resonator, and that some other unaccounted effect was taking place.

5.2 Incompressible Fluid

To quantify the synthetic jet's performance, an estimate of the exit flow velocity and cavity pressure is desirable. The simplest model for analyzing the fluid inside the cavity is to consider the fluid as incompressible. Figure 5.1 shows a cavity having a flexible

vibrating membrane on one side and an opening on the opposite side. The membrane is shown oscillating at its maximum and minimum position. The membrane velocity is V_1, and the exit velocity is V_2. The maximum membrane deflection is referred to as a_0 while the membrane area and opening area are denoted by A_1 and A_2, respectively.

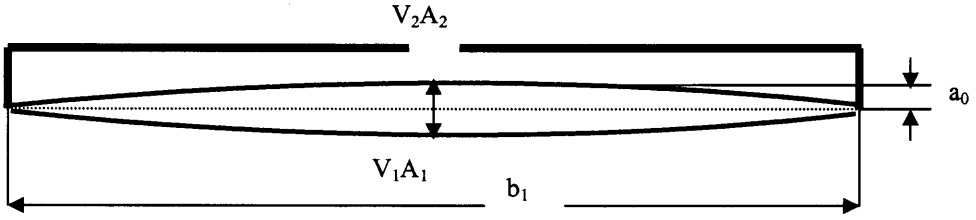

Figure 5.1 Membrane deflection in a sealed cavity with orifice opening.

The membrane deflection and velocity are given by (5.3) and (5.4), respectively

$$w(t) = a_0(t)\cos\frac{\pi x}{2b}\cos\frac{\pi y}{2b} \tag{5.3}$$

$$u(x,y,t) = \dot{w}(t) = \dot{a}_0(t)\cos\frac{\pi x}{2b}\cos\frac{\pi y}{2b} \tag{5.4}$$

A sinusoidal variation of the maximum diaphragm deflection is assumed, i.e.

$$a_0(t) = a_0 \sin\omega t \tag{5.5}$$

$$\dot{a}_0(t) = a_0\omega\cos\omega t \tag{5.6}$$

The volume flux resulting from the membrane deflection is given by equations (5.7)-(5.10).

$$Q(t) = \iint u(x,y,t)dxdy \tag{5.7}$$

$$Q(t) = \iint \dot{a}(t) \cos\frac{\pi x}{2b} \cos\frac{\pi y}{2b} dxdy \tag{5.8}$$

$$Q(t) = a_0 \omega \cos \omega t \iint \cos\frac{\pi x}{2b} \cos\frac{\pi y}{2b} dxdy \tag{5.9}$$

$$Q(t) = \frac{4}{\pi^2} A_D \dot{a}(t) = \frac{4}{\pi^2} A_D a_0 \omega \cos \omega t \tag{5.10}$$

where A_D is the diaphragm area and a_0 the membrane's maximum displacement at the center. Using this result and applying continuity, the velocity can then be determined as a function of the outlet area, A_t.

$$V_2 = \frac{4}{\pi^2} \frac{A_D}{A_t} a_0 \omega \cos \omega t \tag{5.11}$$

Finally, the Reynolds number based on the throat width W can be computed as

$$\mathrm{Re} = \frac{V_2 W}{\nu} \tag{5.12}$$

5.3 Low order Model for Unsteady Flow into the Cavity

The above simple analysis can give a reasonable estimate of the exit velocity. However, both the damping resulting from the volume of air in the cavity and the pressure within the cavity are neglected in the above analysis. The following model overcomes these shortcomings and gives a more complete analysis of the fluid flow in the cavity.

The volume inside the cavity and its time variation due to the deflecting membrane are given by

$$V_D(t) = \iint w(x, y, t) dxdx \tag{5.13}$$

$$V_D(t) = \int_{-b}^{b}\int_{-b}^{b} a_0(t)\cos\frac{\pi x}{2b}\cos\frac{\pi y}{2b}\,dxdy \tag{5.14}$$

$$V_D(t) = a_0(t)\frac{4A_D}{\pi^2} \tag{5.15}$$

$$\dot{V}_D(t) = \dot{a}(t)\frac{4A_D}{\pi^2} \tag{5.16}$$

where V_D is the volume displaced due to the diaphragm displacement.

As presented in Muller et al. (13,14,15) who applied conservation of mass inside the cavity, the resonator's forcing and compliance can be determined using

$$\frac{d(\rho V)}{dt} = \dot{m} = \rho u A \tag{5.17}$$

$$\dot{\rho}V + \rho\dot{V} = \rho u A \tag{5.18}$$

In addition,

$$c^2 = \frac{dp}{d\rho} \tag{5.19}$$

where c is the speed of sound. The resulting solution using the above equations yields an ordinary differential equation (ODE) for the pressure in the cavity.

$$\frac{dp}{dt} = -\rho_{cavity}c^2\frac{u_e A_e}{V} - \rho_{cavity}c^2\frac{1}{V}\frac{dV}{dt} \tag{5.20}$$

The first term on the right hand side represents the cavity compliance and the second term represents the forcing due to the diaphragm motion.

In Figure 5.2, a channel connects the cavity to the outside ambient air. The fluid flows through the channel as it is pulled in and driven out of the cavity.

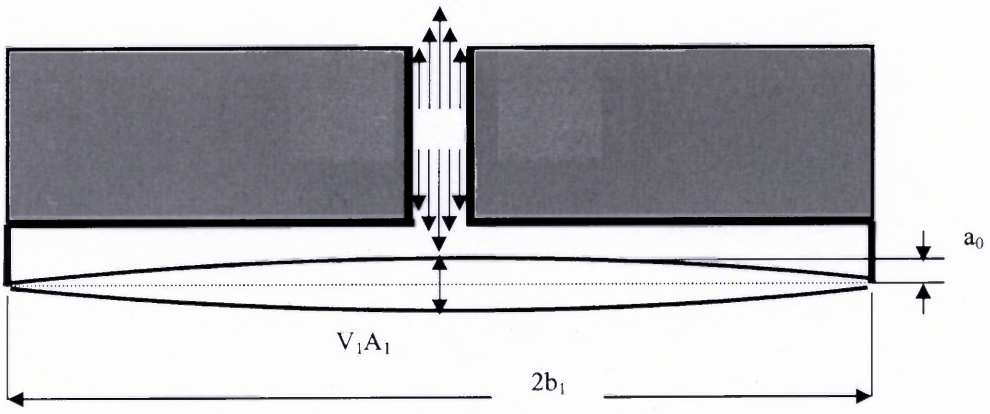

Figure 5.2 Synthetic jet cavity and exit throat.

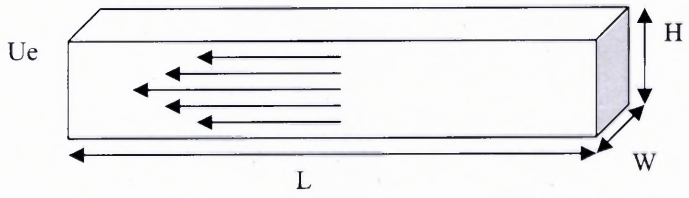

Figure 5. 3 Throat parameters.

The governing equation for the unsteady flow is as follows

$$\rho \frac{D\vec{v}}{Dt} = -\nabla \rho + \mu \nabla^2 \vec{v} \tag{5.21}$$

or, in integral form,

$$\rho \int \frac{d\vec{v}}{dt} \cdot d\underline{s} + \rho \int \nabla \left[\frac{\vec{v}^2}{2} + \frac{p}{\rho} \right] d\underline{s} = \mu \int \nabla \times \vec{\omega} \cdot d\underline{s} \tag{5.22}$$

where the viscous term of the right hand side represents the losses in the throat. For a square channel of uniform cross section, $\nabla \times \omega$ reduces to

$$w_z = -\frac{\partial v_x}{\partial y} \tag{5.23}$$

which, in turn, becomes

$$\frac{\partial w_z}{\partial y} = -\frac{\partial^2 v_x}{\partial y^2} = \frac{1}{\mu}\frac{dp}{dx} \tag{5.24}$$

$$v_{avg} = \frac{h^2}{8\mu}\frac{\Delta p}{L} = \frac{h^2}{8\mu}\frac{dp}{dx} \rightarrow \frac{dp}{dx} = \frac{8\mu v_{\max}}{h^2} \tag{5.25}$$

The exit flow velocity is then given by the following ODE

$$\frac{du_e}{dt} = \frac{p}{L\rho} - \frac{u_e^2}{2C_d^2 L} - 8\frac{\mu u_e W}{\rho H^2 L} \tag{5.26}$$

where U_e is maximum velocity at the exit, p is the difference in pressure in the cavity from the ambient pressure, and ρ and μ are the air density and viscosity, respectively. The discharge coefficient is defined by C_d.

A code was written in MATLAB to solve the two ODEs (equations (5.20) and (5.26)) to obtain a solution for the cavity pressure and exit velocity. During the suction stroke, the following combination of equations holds

$$\frac{dp}{dt} = -\rho_{ambient} c^2 \frac{u_e A}{V} - \rho_{cavity} c^2 \frac{1}{V} \frac{dV}{dt} \tag{5.27}$$

$$\frac{du_e}{dt} = \frac{p}{L\rho} + \frac{u_e^2}{2C_d^2 L} - 8\frac{\mu u_e W}{\rho H^2 L} \tag{5.28}$$

while during the compression (when velocity is positive), the equations were modified to

$$\frac{dp}{dt} = -\rho_{cavity} c^2 \frac{u_e A}{V} + \rho_{cavity} c^2 \frac{1}{V} \frac{dV}{dt} \tag{5.29}$$

$$\frac{du_e}{dt} = \frac{p}{L\rho} - \frac{u_e^2}{2C_d^2 L} - 8\frac{\mu u_e W}{\rho H^2 L} \tag{5.30}$$

A sample solution of the above ODEs is plotted in Figure 5.4 and Figure 5.5. It can be seen that as the frequency is increased the effect of compressibility becomes prevalent. At 10KHz, there is no difference between the simplified incompressible model and the low order compressible model (equations (5.11) and (5.27) through (5.30)). However at 40 KHz the difference becomes clear. The exit velocity for a full range of frequencies is shown in Figure 5.6.

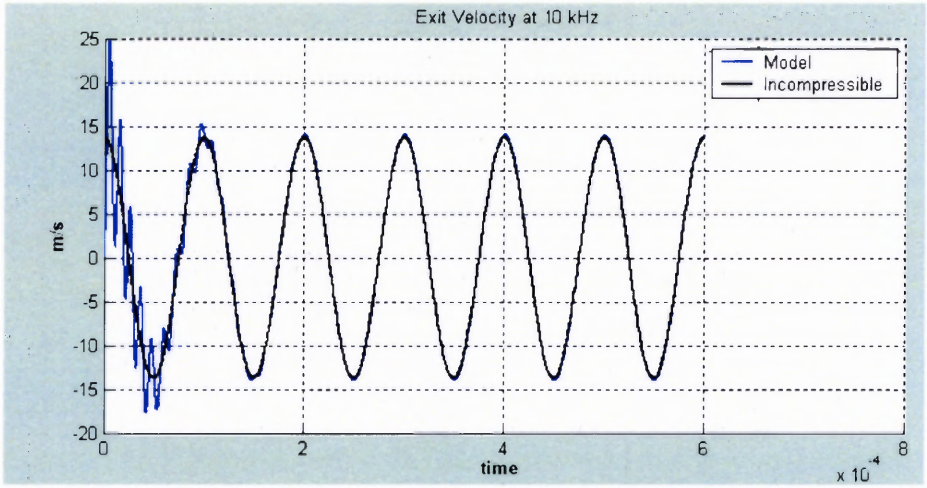

Figure 5.4 ODE solution at 10 Khz.

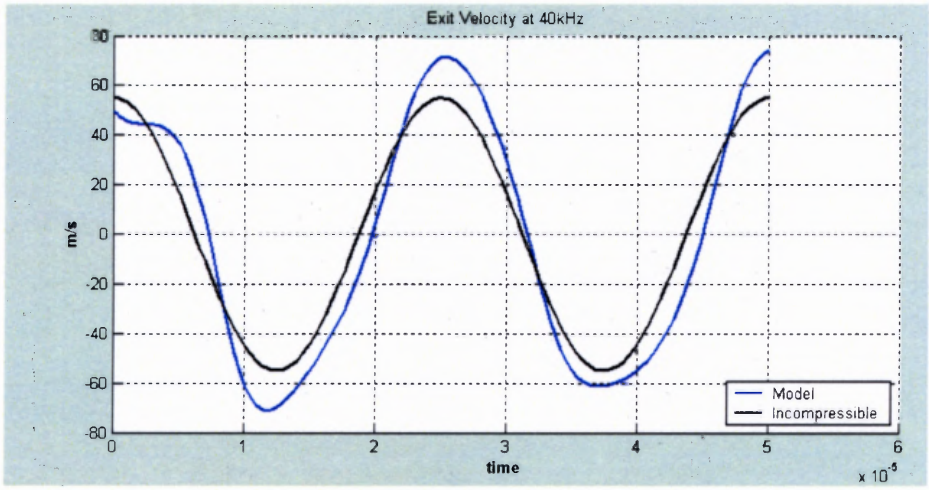

Figure 5.5 ODE solution at 40 Khz.

Table 5.1 Microjet parameters for fluid flow analysis.

Amplitude	15 μm
Cavity height	30 μm
Membrane	3mm x 3mm
Channel Length	360 μm

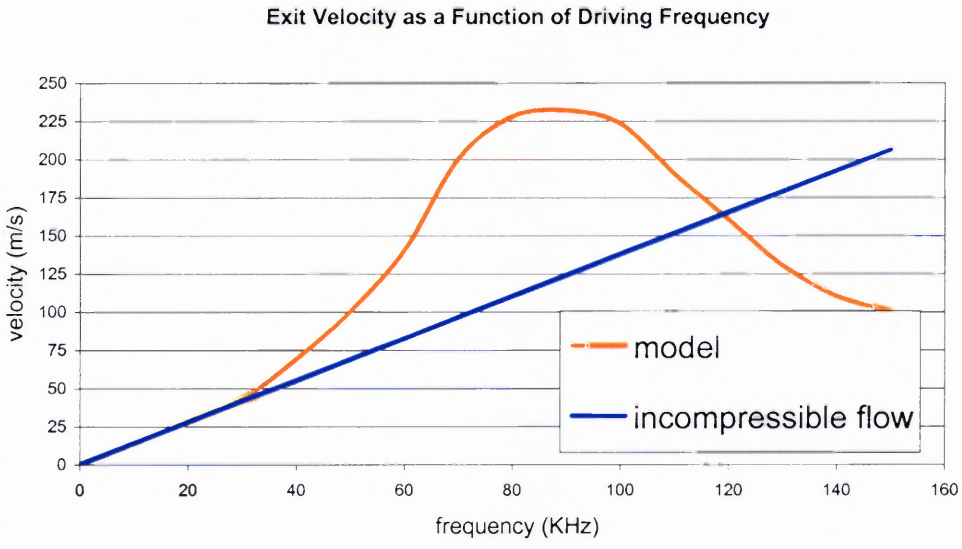

Figure 5.6 Jet exit velocity over a broad range of frequencies.

5.4 Simulation with FLUENT

The fluid flow generated by the oscillating membrane was also studied via Computational Fluid Dynamics (CFD) using FLUENT. The geometry is outlined in Table 5.2. The fluid is considered to be compressible and the membrane motion sinusoidal. This causes the fluid domain to change with the membrane motion. Therefore, an adaptive mesh is prescribed in the cavity to account for the unsteady change in cavity

volume. The boundary conditions on the side walls of the cavity are taken as no slip. In the far field, atmospheric pressure is assigned.

In Figure 5.8 vorticity levels are displayed for once cycle of the membrane oscillation. The plots of vorticity closely resemble the flow fields presented in Chapter 2. However, the simulation permits the detailed analysis of the fluid flow at any time during the cycle. It is clear that by the time $t = 3\pi/2$, strong vortical structures are present in the cavity as well as downstream, the vortices propagating downstream as they are pinched at the edges.

It should be noted that this is not a fully coupled solution to the problem, as the membrane is given a prescribed motion, which is not affected by the fluid inside the cavity.

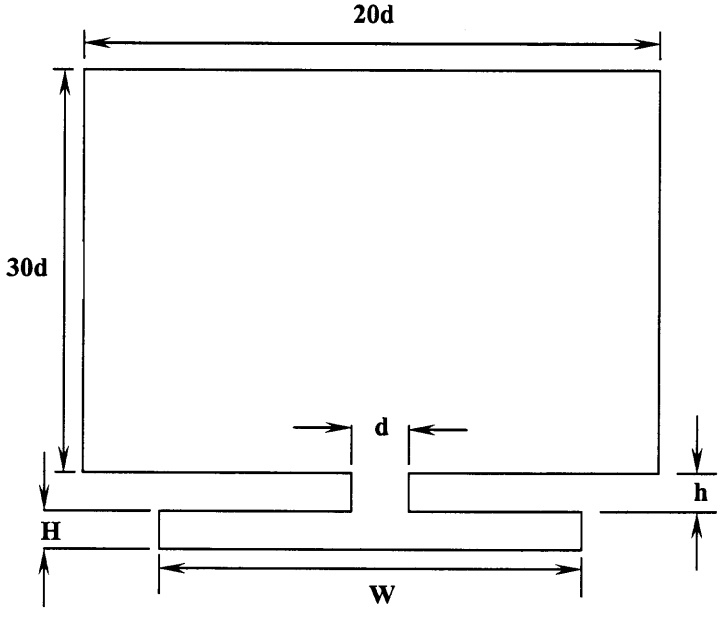

Figure 5.7 Geometry used for the synthetic jet simulation.

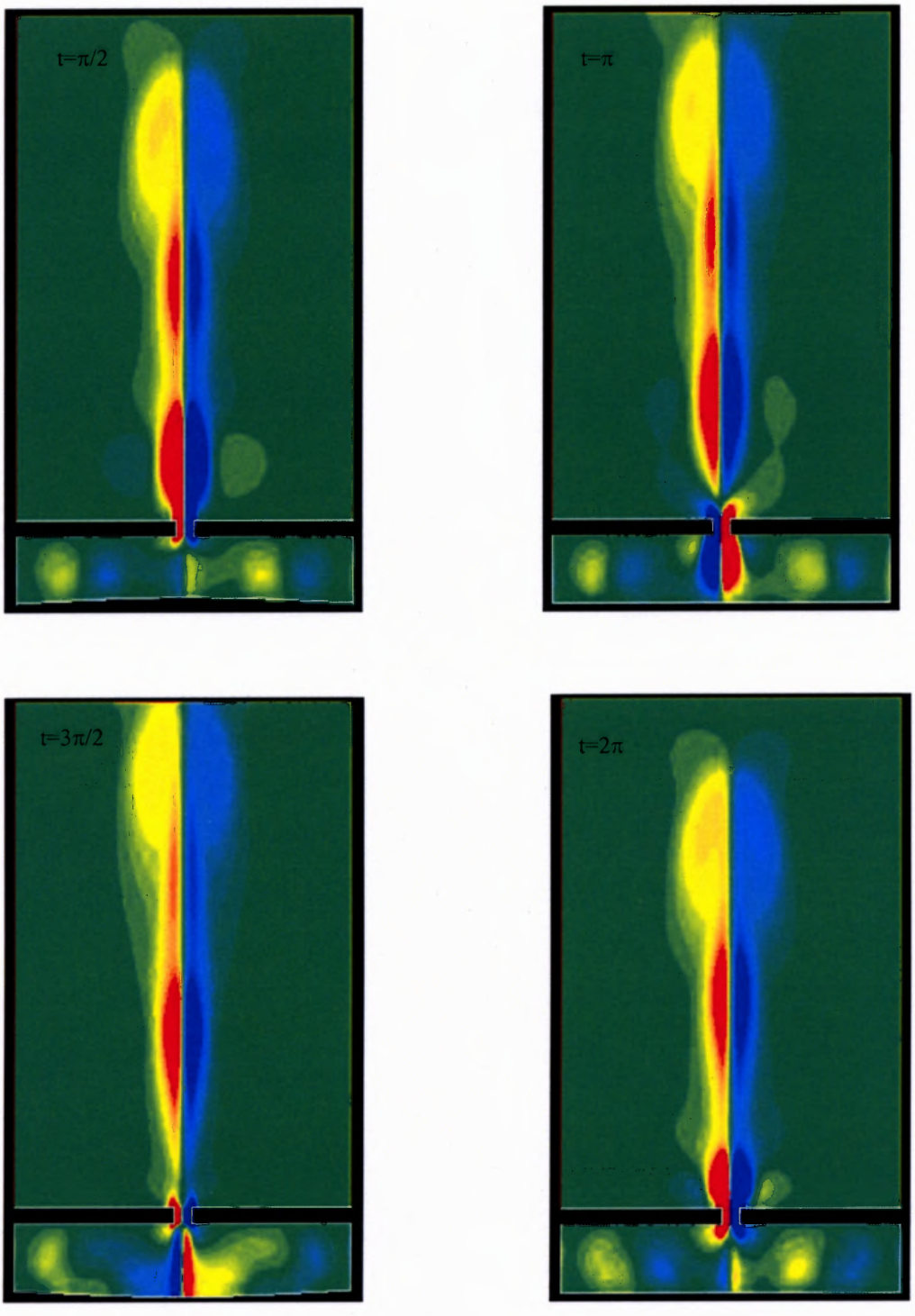

Figure 5.8 2D Vorticity contour levels from the FLUENT numerical simulation of the synthetic jet.

Table 5.2 Values used for the synthetic jet simulation of Figure 5.8.

d = 500 μm	A = 200 μm
Amplitude = 0.4d	h = 500 μm
h/d = 1	H = 2000 μm
A/H = 0.1	W = 10,000 μm
W/H = 5	ω = 1000 Hz

Some studies were also conducted in three dimensions. The velocity at the exit is plotted as a function of frequency in Figure 5.9 and compared to that obtained with the low order model. For the parameters chosen (Table 5.3), there is good agreement at low frequencies between the incompressible and compressible models/numerical simulations. However, as the frequency increases, compressible effects become important and some differences appear. Both the CFD and low order model show a peak in performance at a certain frequency value and then a sharp drop off as frequency increases. Notice that such peak is absent when the fluid is considered incompressible. It is then clear from the results that the peak performance is not only associated with the resonant frequency of the membrane, but is some function of the fluid inside as well.

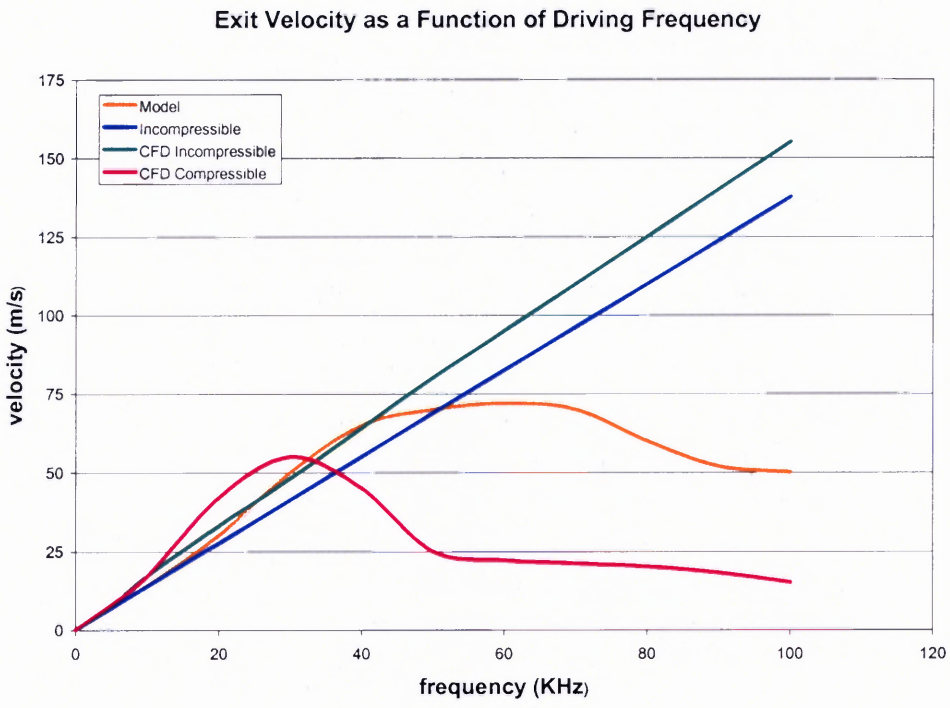

Figure 5.9 Comparison of incompressible model, low order model, and 3D numerical compressible and incompressible simulations using FLUENT.

Table 5.3 Values used in the 3D FLUENT simulations.

Amplitude	15 μm
Cavity height	300 μm
Membrane	3mm x 3mm
Channel Length	90 μm

5.5 Squeeze Film Analysis

If the cavity is very thin with respect to the length of the membrane, the squeeze film of the fluid must be considered. Under such conditions, the fluid can exert huge pressures against the cavity, greatly hindering its motion and requiring huge voltages to excite. For simplicity, it is assumed that the membrane deformation is in the normal direction only.

The analysis begins with the compressible Reynolds gas-film equation, which can then be linearized and non-dimensionalized (3).

$$\nabla^2\psi - \sigma\frac{\partial\psi}{\partial\tau} = -\sigma\varepsilon\sin\tau \tag{5.31}$$

where σ is the squeeze film number, defined as

$$\sigma = \frac{12\mu a^2}{p_a g_0^2}\omega \tag{5.32}$$

The displacement amplitude is given by the term ε, which is $\varepsilon = \frac{a}{g_0}$. (Note: ε is the same as $\bar{a}$ in equation (4.9)) The non-dimensional pressure perturbation is given by ψ. Using a finite element PDE solver, the pressure perturbation, ψ, at all points on the surface can be determined. Assuming that there is no orifice in the center for the fluid to flow through, the boundary conditions for the squeeze film problem are shown in Figure 5.10.

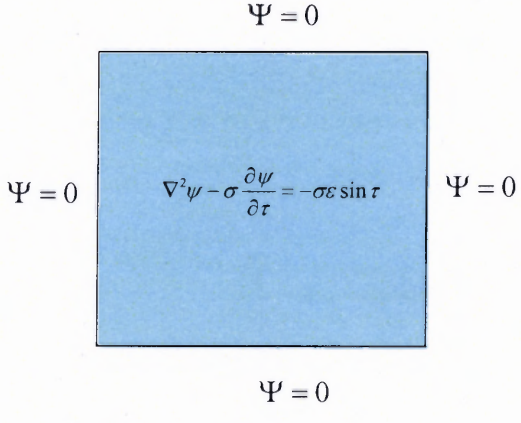

Figure 5.10 Finite element PDE solver Boundary conditions for determining the pressure perturbation.

Alternatively, more insight can be gained by analyzing equation (5.31) further. A solution of the following form is assumed for the pressure distribution

$$\psi = \psi_1 \cos\tau + \psi_0 \sin\tau \tag{5.33}$$

The pressure distribution has two components, ψ_1 and ψ_0, representing the fluid spring force and the viscous damping force, respectively. Equation (5.33) can be substituted into equation (5.31) above. Collecting the sinτ and cosτ terms gives

$$\nabla^2\psi_1 - \sigma\psi_0 = 0 \tag{5.34}$$

$$\nabla^2\psi_0 - \sigma\psi_1 = -\sigma\varepsilon \tag{5.35}$$

Blech (3) expands the solutions Ψ_0 and Ψ_1 as follows:

$$\begin{aligned} \psi_0 &= \varepsilon \sum_{\substack{m,n \\ odd}} a_{mn} \cos m\pi X \cos n\pi Y \\ \psi_1 &= \varepsilon \sum_{\substack{m,n \\ odd}} b_{mn} \cos m\pi X \cos n\pi Y \end{aligned} \tag{5.36}$$

where the coefficients a_{mn} and b_{mn} are given by

$$\begin{aligned} a_{mn} &= \frac{16\sigma(-1)^{\frac{m+n}{2}}}{\pi^4} \frac{\left[m^2 + n^2c^2\right]}{mn\left[\left(m^2 + n^2c^2\right)^2 + \frac{\sigma^2}{\pi^4}\right]} \\ b_{mn} &= \frac{16\sigma^2(-1)^{\frac{m+n}{2}}}{\pi^6} \frac{1}{mn\left[\left(m^2 + n^2c^2\right)^2 + \frac{\sigma^2}{\pi^4}\right]} \end{aligned} \tag{5.37}$$

The above equations are then solved and plotted using MATLAB. The solutions of the set of equations (5.36) for varying frequencies are shown in Figure 5.11. As seen from

the series of pictures in Figure 5.11, at low frequencies the highest pressure is concentrated in a circular area near the center. As frequency increases, the high pressure concentration occupies a square-like region, filling out the entire area. It is also noteworthy that the maximum pressure value decreases as frequency increases, as it is clear in Figure 5.12.

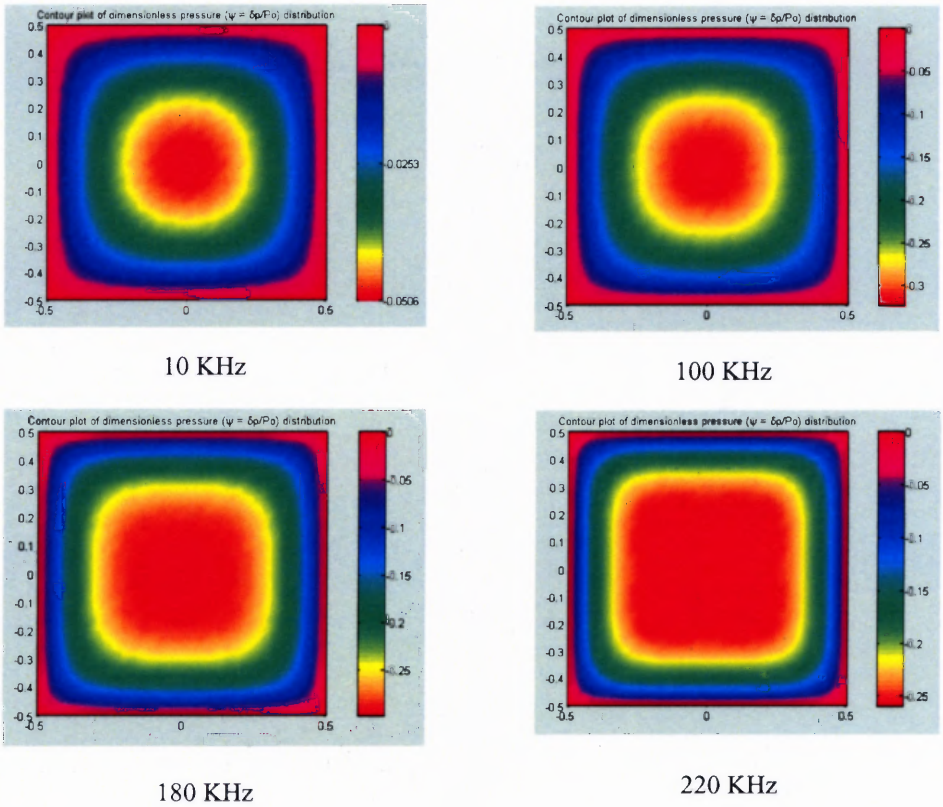

Figure 5.11 Pressure distribution for increasing frequency.

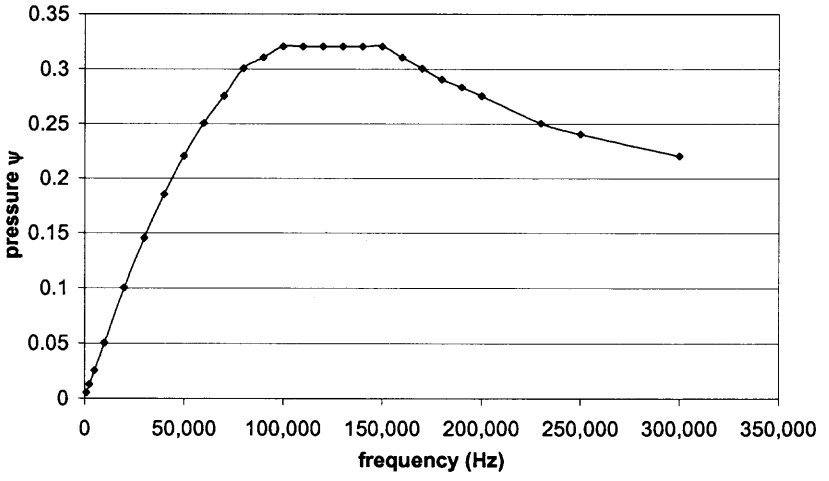

Figure 5.12 Maximum cavity pressure as a function of plate frequency.

The set of equations (5.36) can be solved analytically and then used to solve equation (5.33). The non-dimensional damping and spring forces are given by

$$f_0 = \frac{1}{A}\int_A \psi_0 dA \qquad \text{Damping Force}$$
$$f_1 = \frac{1}{A}\int_A \psi_1 dA \qquad \text{Spring Force} \tag{5.38}$$

with the fluid damping coefficient being defined as

$$C_f = \frac{f_0\, p_a A_m}{a_m \omega} \tag{5.39}$$

where the denominator represents the membrane velocity. Likewise, the stiffness coefficient is defined as

$$K_f = \frac{f_1\, p_a A_m}{a_m} \tag{5.40}$$

The frequency at which the damping and stiffness coefficients are equal is also known as the cut-off frequency. At low frequencies, fluid damping is more prevalent. Above the cutoff frequency, the fluid acts more like a stiff spring. Equations (5.39) and (5.40) will be used in the following chapter to describe the one-dimensional equation of motion for the system.

For the sealed cavity with an orifice, the boundary conditions for the squeeze film equation can be applied as shown in Figure 5.13. For the membrane, the variation in the gap spacing is $\cos \pi X \cos \pi Y$. The contour plots in Figure 5.14 allows the comparison between the result of the 3D numerical simulation and that obtained from the squeeze film equation solved with a PDE solver (FlexPDE). The slight differences in the magnitude of the pressure are due to the simplistic boundary condition $\psi = 0$ imposed at

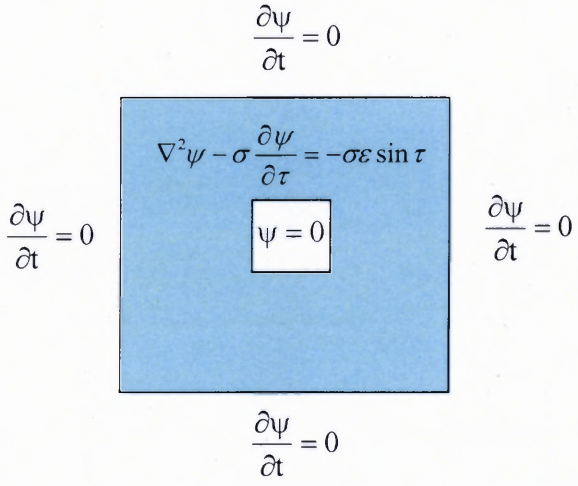

Figure 5.13 Boundary conditions for a sealed cavity with orifice.

the orifice. The approximation can be improved by accounting for the losses and resistance through the channel and the orifice.

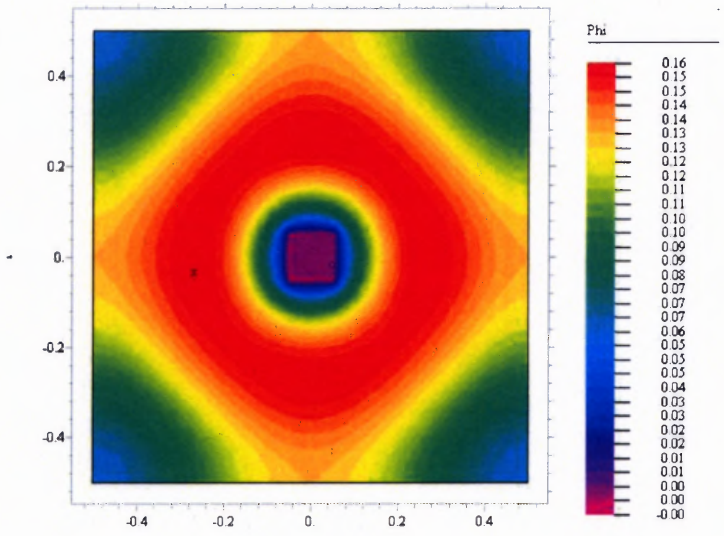

a. Solution obtained from the non-dimensional squeeze film equation

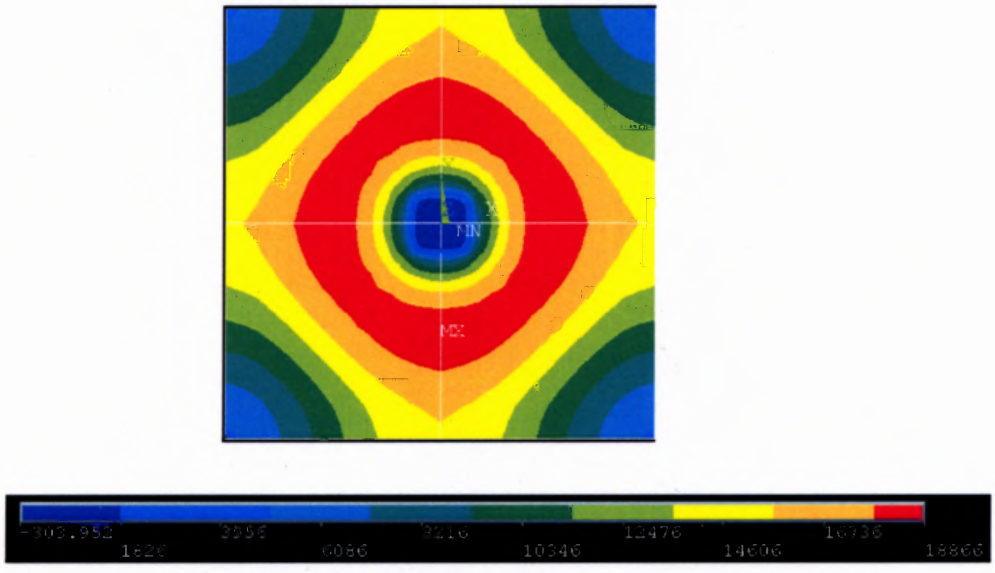

b. Full numerical solution of the coupled fluid-structure interaction.

Figure 5.14 Comparison of pressure contours between the full numerical simulation and the squeeze film equation. The parameters taken are f = 20KHz, $\varepsilon = 0.4$, gap = 10μm, $t = \pi/2$.

The fluid flow through the nozzle is studied by running a full numerical simulation of the fluid subject to a sinusoidal fluctuation of the membrane. The fluid

inside the cavity is assumed to be compressible. The geometry of the jet is symmetric, therefore only one quarter is considered. The boundary conditions are applied as shown in Figure 5.13 and the model mesh is displayed in Figure 5.15. The large gradients near the wall require a very fine mesh to accurately capture the flow velocity profile. An Arbitrary Lagrangian-Eulerian (ALE) Formulation is employed for moving the mesh in the cavity.

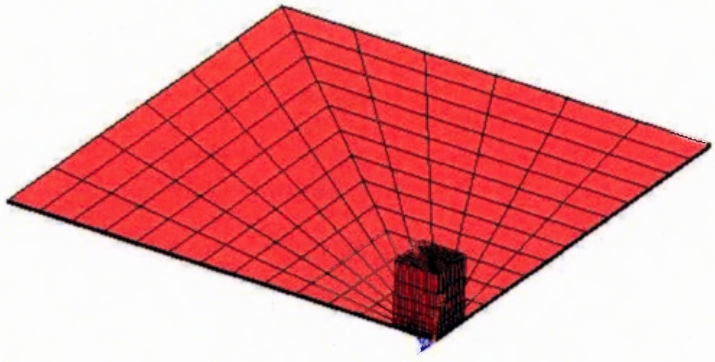

Figure 5.15 Quarter model mesh for the simulation of the microjet.

In Figure 5.16, it is observed that the fluid is squeezed between the membrane and the upper cavity wall. Near the channel, the fluid accelerates considerably at the boundary of the cavity and the channel.

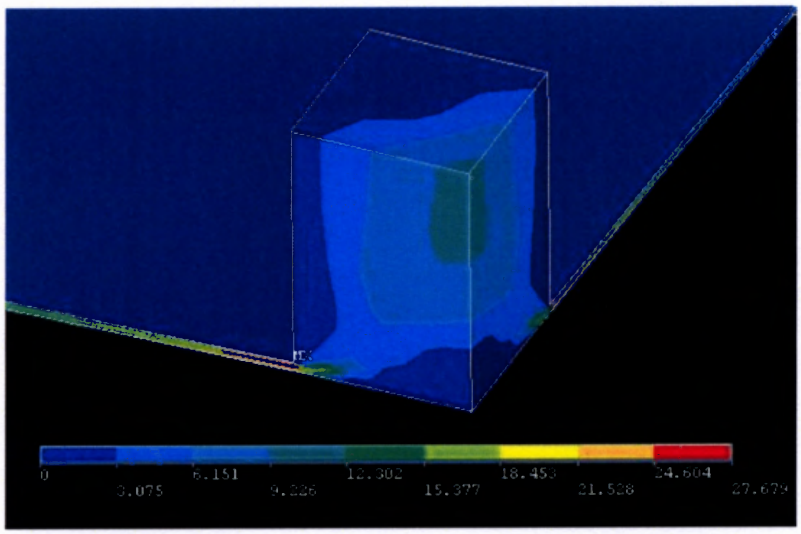

Figure 5.16 Velocity contours through the nozzle for the following values of the parameters: f = 20KHz, ε = 0.4, gap = 10μm.

In the series of plots in Figure 5.17, the velocity across the exit plane of the orifice is plotted as a function of frequency and time. For all but the highest frequency, there is always a flow in the positive direction near the center of the orifice. However, between t = $\pi/2$ and t = 2π, there is also flow in the opposite direction going into the cavity. This negative flow could result in shearing the main flow exiting the orifice, which could induce vorticity at the orifice.

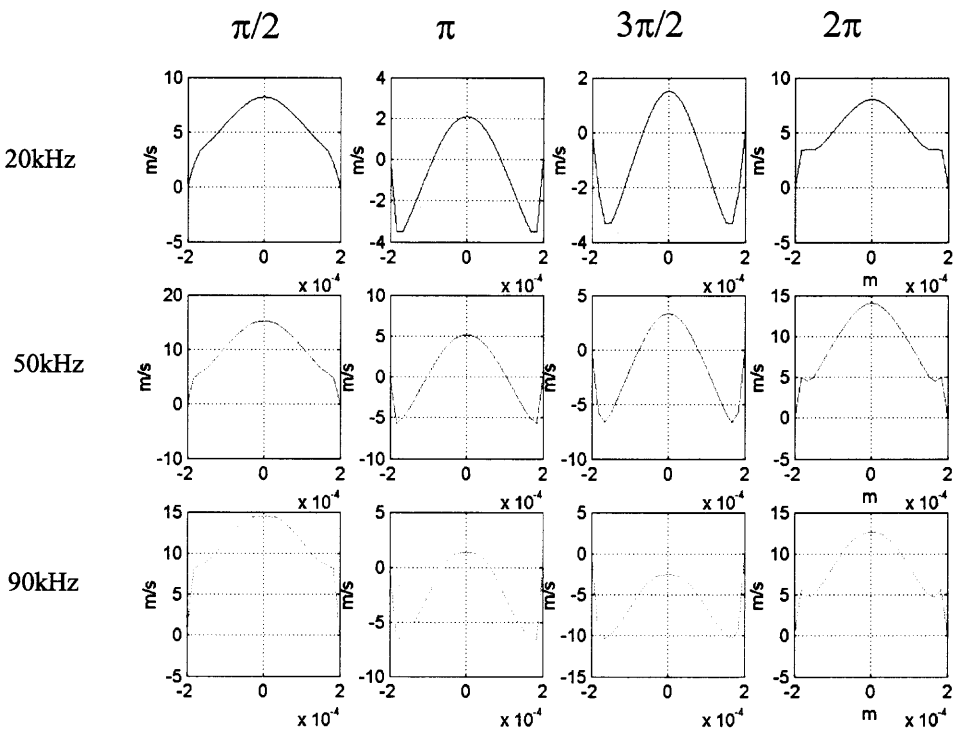

Figure 5.17 Velocity profile at the channel exit.

5.6 Power to Overcome Fluid Pressure

The average power required to drive the membrane at a prescribed amplitude is given by the average of the integral (over the period) of the product of the force and the velocity. The force is twice the pressure required to displace the membrane multiplied by the surface area of the membrane. When the membrane is compressed (decrease in cavity volume and positive velocity), the face of the membrane exposed to the open air experiences a suction, thus causing the membrane to resist deflection. The force required

to overcome the negative backpressure (suction) is equal to the force required to deflect the membrane inside the cavity. The average power can then be expressed as

$$P = \frac{2}{T}\int_0^T p^*(\cos\omega t)(u\cos\omega t)Adt \tag{5.41}$$

where $p^* = c\rho u$ and $T = 2\pi/\omega$, the period of oscillation. Once integrated, the average power can be calculated according to

$$P = c\rho u^2 A = c\rho A a_0(t)\omega^2 \tag{5.42}$$

Here, the speed of sound is given by c, ρ is the density of the ambient fluid, and the membrane area is A. The velocity at the center of the membrane, u, is rewritten in terms of $a_0(t)$, the maximum center displacement, and frequency of oscillation, ω. This power is in addition to the power required to drive the membrane, discussed earlier in Chapter 3.

CHAPTER 6

LOW DIMENSIONAL MODEL

6.1 Coupling of Forces

The fluid flow generated by a synthetic jet is the result of the complex coupling between the mechanical forces of the deformed membrane, electrical forces from the actuation, and the forces of the fluid in motion. In the previous three chapters each of these forces has been addressed individually. This gives great insight into the individual parameters and their interrelationships. From a practical point of view, it is very desirable to have, for example, the exit velocity of the jet as a function of the applied voltage. A transfer function is especially necessary if the actuator is to be used as part of a control loop, in which the input (voltage) to output (fluid velocity) must be precisely known prior to applying the control. Therefore, it is necessary to study the effect of these forces when they are combined. Solving the coupled equations rigorously is computationally expensive, requiring long run times, and thus often impractical. Numerical simulations are difficult to set up and require complex software and codes. A low dimensional model can be extremely useful in capturing the primary actuator dynamics. In the previous chapters it was shown that the complexity of the full three-dimensional solutions of the independent problems can be simplified to lower order models. The goal of this chapter is to combine the various reduced models and compare the integrated model to full numerical simulations that solve the coupled equations directly.

6.2 Equation of Motion

The equation of motion can be used to fully couple the forces in a dynamic setting. The structural damping of the membrane is small compared to the other forces, and is therefore ignored. The equation of motion for the system can be written as

$$m\ddot{a} + ka + F_f + F_e = 0 \tag{6.1}$$

where m is the mass of the membrane, k is the membrane's stiffness, F_f is the fluid pressure, and F_e is the external pressure on the backside of the membrane, in this case the electrostatic pressure that drives the membrane. Equation (6.1) can be rewritten as

$$\ddot{a} + \frac{k}{m}a = -\left(\frac{F_e + F_f}{m}\right) \tag{6.2}$$

The substitution for the natural frequency can be made

$$\omega^2 = \frac{k}{m} \tag{6.3}$$

Substituting and rearranging terms yields

$$m\left(\ddot{a} + \omega^2 a\right) = -\left(F_e + F_f\right) \tag{6.4}$$

while integrating over the membrane area leads to

$$\bar{m}\left(\int\int \ddot{a}\, dxdy + \int\int \omega^2 a\, dxdy\right) = -\left(\iint p_e dxdy + \iint p_f dxdy\right) \tag{6.5}$$

where $\bar{m} = \rho t$ is the mass per unit area. The result is then

$$\bar{m}\frac{4A_m}{\pi^2}\left(\ddot{a}+\omega^2 a\right)=-\left(p_e A_m + p_f A_m\right) \tag{6.6}$$

For the steady case, the acceleration and fluid pressure terms drop out, which leaves

$$\bar{m}\frac{4A_m\omega^2 a_m}{\pi^2}=-p_e A_m \tag{6.7}$$

As previously shown, for small amplitude, the stable limit is $\bar{a} = 0.542$. This is substituted into equation (4.12) . Solving for p_e and substituting into (6.7) the pull-in voltage can be estimated.

$$\bar{m}\frac{4\omega^2 a_m}{\pi^2}=\frac{\varepsilon V_{in}^2}{2g_0^2}\frac{1}{(1-\bar{a})^{.846}} \tag{6.8}$$

$$V_{pi}^2=\bar{m}\frac{8\omega^2 g_0^3}{\varepsilon\pi^2}\bar{a}(1-\bar{a})^{.846} \tag{6.9}$$

$$V_{in}=\frac{1.5\omega}{\pi}\sqrt{\frac{\bar{m}g_0^3}{\varepsilon}} \tag{6.10}$$

Adding the effect of the fluid, the equation of motion becomes

$$m\left(\ddot{a}+\omega_n^2 a\right)=-\left(F_e + C_f\,\dot{a} + K_f\,a\right) \tag{6.11}$$

Taking into account the expression of the various coefficients in the former equation, one obtains

$$m\left(\ddot{a}+\omega_n^2 a\right)=-\left[\frac{A_m}{2g_0^2}\frac{\varepsilon V_{in}^2}{(1-\bar{a})^{.846}}\right]-\left[\frac{64\sigma\, p_a A_m}{\pi^6 g_0 \omega}\sum_{m=odd}\sum_{n=odd}\frac{\left[m^2+n^2c^2\right]}{(mn)^2\left[\left(m^2+n^2c^2\right)^2+\frac{\sigma^2}{\pi^4}\right]}\right]\dot{a}- \tag{6.12}$$

$$\left[\frac{64\sigma^2\, p_a A_m}{\pi^8 g_0}\sum_{m=odd}\sum_{n=odd}\frac{1}{(mn)^2\left[\left(m^2+n^2c^2\right)^2+\frac{\sigma^2}{\pi^4}\right]}\right]a$$

Figure 6.1 depicts the time variation of the membrane position at the center for a frequency of 100Hz. As expected, at such a low frequency the fluid effects are negligible, and the membrane simply follows the electric field. The electric field being always positive, the membrane position is always possible and the membrane oscillates at a frequency whose value is double that of the driving electric field.

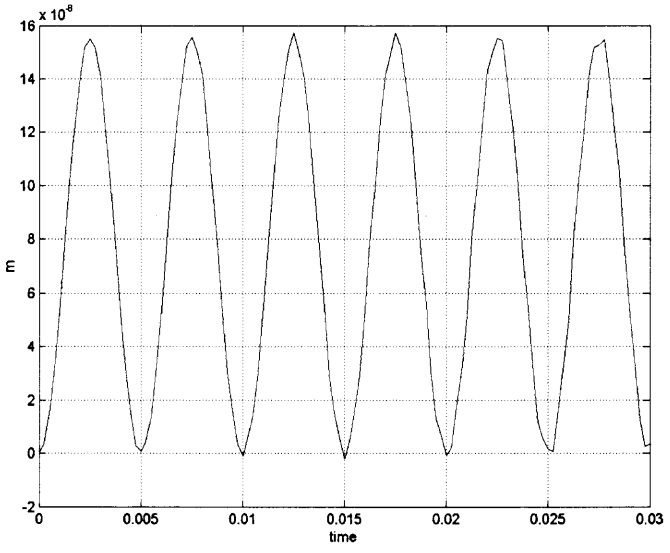

Figure 6.1 Time variation of the membrane position at the center for a frequency of 100Hz computed from the low order model coupling the electric field and membrane deformation.

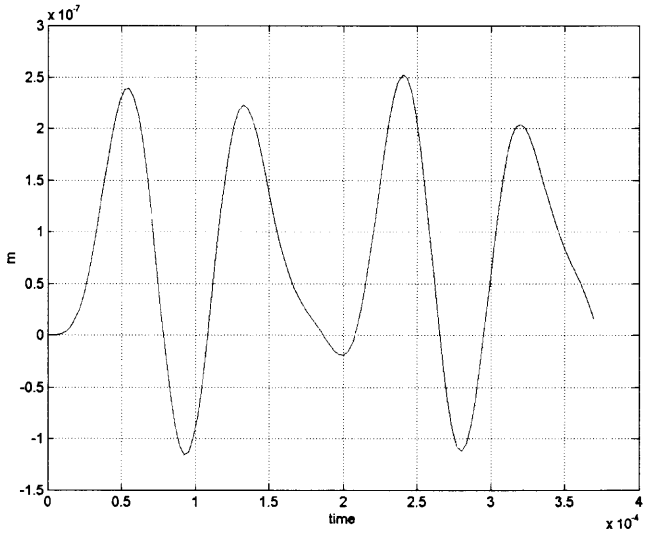

Figure 6.2 Time variation of the membrane position at the center for a frequency of 8124 Hz computed from the low order model neglecting the influence of the fluid flow.

In Figure 6.2, the drive frequency is increased to the value of 8124Hz, which corresponds to the natural frequency of the membrane. To study the membrane response to the electric field alone, the fluid is neglected. Because the electric field is always positive and attractive, the motion of the membrane is not in phase with the drive frequency. The membrane position is negative for part of the cycle and the amplitude is four times lower than at the lower frequency of 100Hz. The electric field can introduce other modes of vibration, which the low order model cannot fully capture. The damping and spring effects of the fluid tend to supress higher modes very early in the cycle. Because the membrane responds by oscillating at its fundamental mode, it is possible to capture the membrane motion with a one-dimensional model.

A comparison between the full numerical simulation and the low order model is presented in Figure 6.3. In this example, the system is clearly over damped. The membrane is initially attracted to the fixed electrode, but then it becomes stuck in the upper position. The membrane oscillates with very low amplitude. Although the 1-D model does not lead to an exact match with the full numerical simulation, it clearly captures the dynamical system's response to the electric field. Where a numerical simulation can take days to run for just a few cycles, the 1-D model can be solved in seconds. The model can be effective in signaling out which particular parameters to study more rigorously with numerical methods.

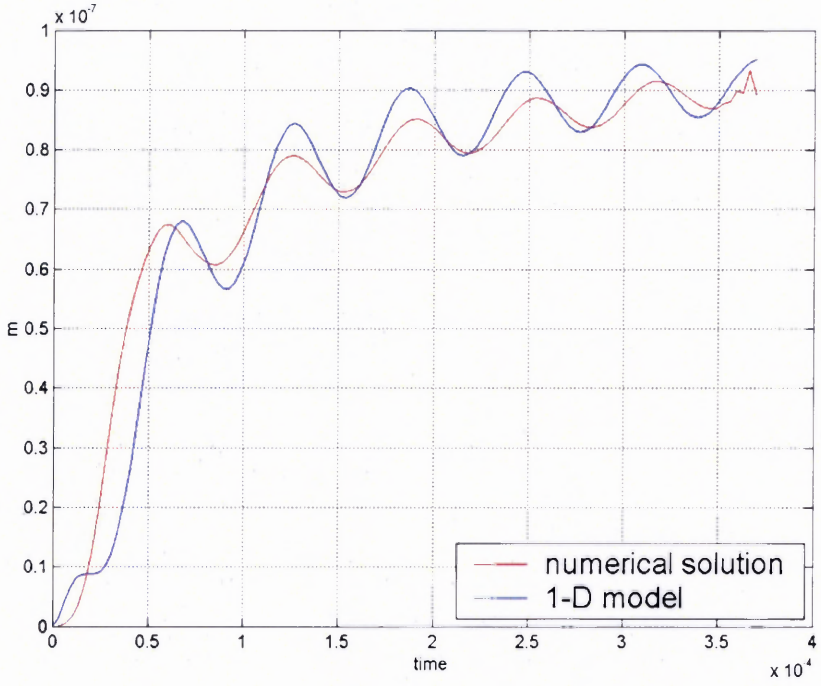

Figure 6.3 Time variation of the membrane position at the center computed by means of the full numerical simulation and the 1-D model including the electric field - fluid -structure interaction at a frequency of 8124Hz.

CHAPTER 7

MEMS FABRICATION

The synthetic microjet was fabricated by bonding two 8", 380 μm thick silicon wafers. By creating the membrane on a separate wafer, complications, such as stiction, associated with releasing thin structures, was avoided. Both wafers were preprocessed with a layer of oxide and nitrite on all faces. The cavity and throat were also fabricated each on separate wafers. Standard selective wet etching of silicon can be used to create the cavity. An advantage to using a wet process is that expensive machinery is not required, and processing does not necessarily need to take place strictly in a clean room environment. Access to dry etching machines, such as Deep Reactive Ion Etching (DRIE), is typically difficult and expensive. A disadvantage of wet etching, however, is that the final feature is limited to square or rectangular geometries. In addition, the sloped sides that result from wet etching are not always desirable. Anisotropic wet etching results in a microdiffuser in place of a straight-walled channel. Subsequently, much of the jet's energy would be lost. The membrane, cavity, and channel were therefore created in a dry etch process.

Boron diffusion was used to stop the etching at the desired membrane thickness. Typical membrane thicknesses range from 5 μm to 15 μm. The nitrite that was used for the etch mask was stripped off just prior to bonding. The oxide layer remains and acts as the insulator between the two wafers once they were bonded.

The two-wafer sandwich is divided into 4 equal quadrants. Starting on the top-right quadrant of the membrane side, the membrane sizes range from 5^2 mm^2 to 2^2 mm^2,

as shown in Figure 7.1a. On the opposite side, the minimum channel dimensions are arranged and incremented as shown in Figure 7.1b. The wafer is diced for the testing of individual jets. The fabrication was carried out at the Lucent Micro Fabrication Facility in Murray Hill, New Jersey. The process flow is shown in the figure series of Figure 7.2.

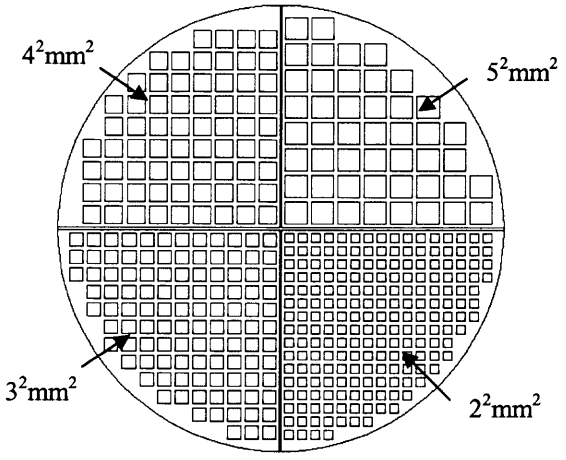

(a) Membrane wafer

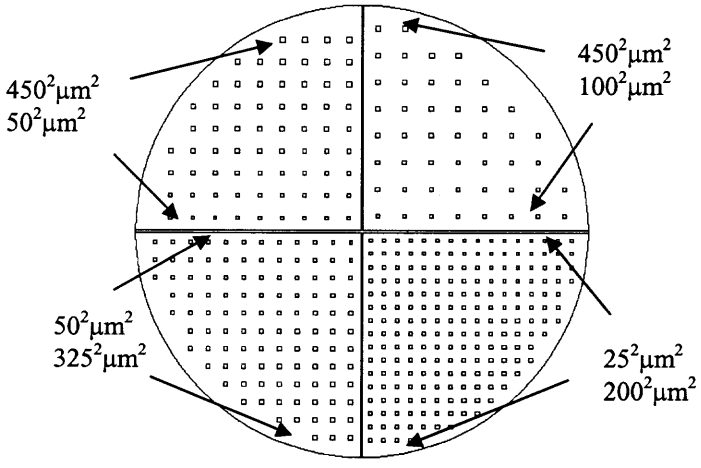

(b) Nozzle wafer

Figure 7.1 Front and back layout of the device showing the two 4" bonded wafers before dicing.

WAFER 1: JET CAVITY AND NOZZLE

Starting Material:

Silicon Wafer: 8"

Approximately 350 μm thick

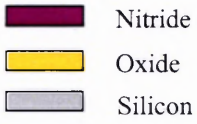

1.

- Clean Wafers
- Wet Oxidation. Target 3000A
- Silicon Nitride. Target 2500A

2.

- Apply photo resist on front

3.

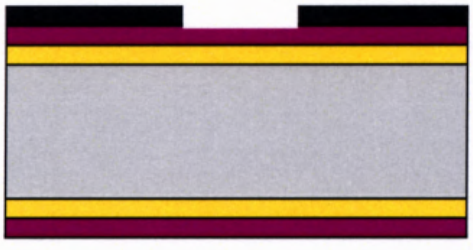

- Align and expose mask for front etch
- Develop

4.

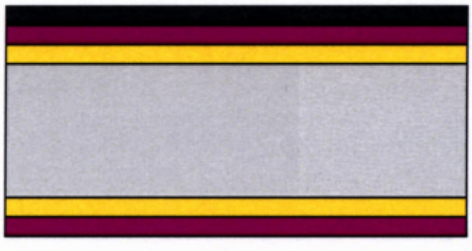

- Dry etch nitride and oxide

5.

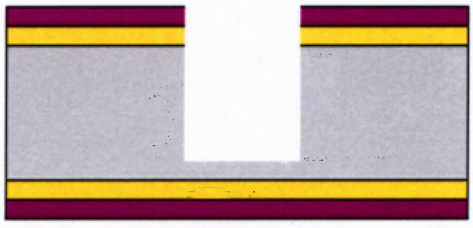

- Strip PR
- Dry or wet etch through silicon (leave approx. 10μm)

6.

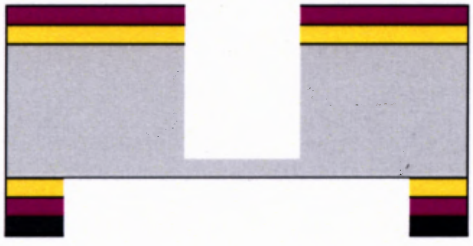

- Apply Photo Resist to other side
- Align and expose mask for backside etch
- Dry etch nitride and oxide

7.

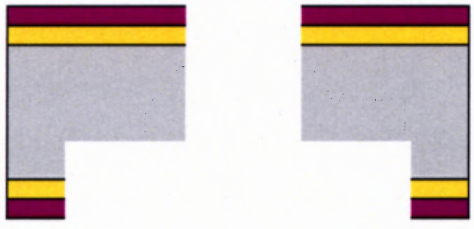

- Dry or Wet Etch silicon. Target: 10-40 μm

8.

- Strip nitride

WAFER 2: MEMBRANE

Starting Material:

Silicon Wafer: 8"

Approximately 350 μm thick (or less by shaving)

9.

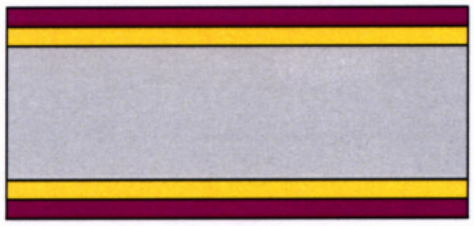

- Clean wafers
- Wet Oxidation. Target 3000A
- Silicon Nitride. Target 2500A

10.

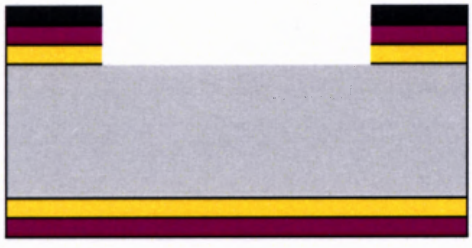

- Apply Photo Resist
- Align and expose mask for front etch
- Develop
- Etch nitride and oxide

11.

- Etch through silicon, creating a 10-40 μm thick membrane

12.

- Strip wafer

13. 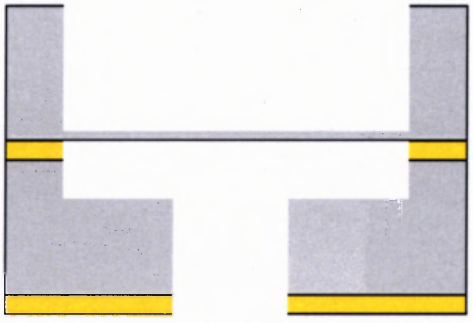

- Align and bond wafers

Figure 7.2 Process flow for the fabrication of the synthetic microjet.

Figure 7.3 shows the etched nozzle wafer. The section of the wafer has been cut in half to show the detail of the nozzle and cavity. Figure 7.4 shows a close-up view of the nozzle.

Figure 7.3 Cutaway section of nozzle wafer showing nozzle and cavity.

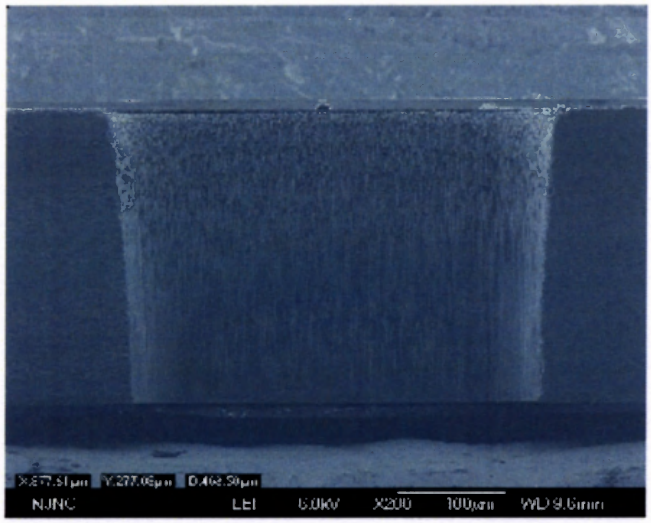

Figure 7.4 Close-up view of nozzle and channel.

CHAPTER 8

CONCLUSION AND FUTURE STUDIES

A vibrating plate in a sealed cavity with a small opening can be used to generate a jet flow. The jet is created from the fluid surrounding the actuator and is of zero net-mass flux. A miniature synthetic jet has been fabricated and tested. The jet has been visualized for varying excitation frequencies of the driver. As the images in Chapter 2 show, the characteristics of the jet can vary over a range of drive frequencies. At low frequencies distinct streaks are present and the jet is well defined. As the frequency is increased, the jet becomes more turbulent and less cohesive. A curious observation was made in that there are ranges of frequencies in which no jet was observed. By altering slightly the drive frequency, a jet can thus be created or destroyed. The displacement, or stroke, of the driver varies with the drive frequency, and cannot be decoupled.

Experiments were conducted to test the jet as an electronic cooling alternative. Temperature measurements show that for the cases studied, by impingement of the jet on a concentrated heat source, a substantial reduction in heat can be achieved. The jet was found to be more effective at cooling than a comparable sized heat sink alone. Future studies should concentrate on deriving nondimensionalized parameters that can quantify the optimized placement of the jet relative to the heat source. The effect of baffling, the degree of cooling that can be achieved in sealed or nearly sealed enclosures, and tripping of the boundary layer of a crossflow created by a fan should be studied further. In particular, tripping the boundary layer with the synthetic jet has great promise in enhancing the cooling effectiveness of fans alone.

In Chapters 3, 4, and 5 the membrane mechanics, electrostatic actuation, and fluid dynamics, respectively, were each studied separately in detail. Most noteworthy is that a squeeze film approach is used to quantify the cavity pressure of the microjet. The cavity pressure generates the pressure head to drive the fluid into and out-of the cavity. Due to the squeeze film action, acoustic effects in the cavity are not applicable. The pressure in the cavity generates the head that drives the fluid through the cavity. Simulations indicate that there is always a positive mean flow in the center of the channel. The fluid entering the cavity stays near the walls of the channel. This adjacent positive and negative vectored flow could shear the mean flow through the channel, which could induce vortex formation near the orifice. The flow field just downstream of the orifice for the microjet was not studied here, but should be studied in more detail in future works.

In Chapter 6 the separate physics of the previous three chapters are combined to derive a closed one-dimensional transfer function that can capture the prevalent dynamics of the system. The inputs to the model are the voltage amplitude and driving frequency. The function was solved for the membrane displacement in time. The dynamical system was also solved using Ansys Multi Physics. When compared to the Ansys simulation, the transfer function captures the main features of the system response. However, the one-dimensional model is a powerful tool in that it can greatly reduce the computational time required to evaluate and predict the jet efficiency for a given set of parameters. Once the desired response has been identified with the model, the system can be studied in more detail using more rigorous and precise numerical methods. The preliminary results presented in Chapter 6 indicate that for the parameters chosen, the system tends to be

over damped. A more complete study should be conducted to identify parameters, such as the drive function, which can give the optimum displacement response of the membrane. Indications are that a slightly "tweaked" sine function can give a more desirable response. In addition, a square pulse input function was not studied at this time; however, a detailed analysis should be carried out in the future.

Lastly, in Chapter 7 a design for fabricating a micro-sized synthetic jet actuator is presented. The primary design element is that the membrane and cavity with channel are created on separate wafers. The wafers are then bonded together. This avoids complications which arise in releasing thin structures. This also allows more control in the dimensions and tolerances for the membrane thickness and cavity height. Finally, some images of the fabricated device are shown at the close of the chapter.

In this study, the fabricated jet was not yet tested. As a first step, a static analysis of the membrane displacement should be conducted and membrane actuation demonstrated. Once it has been demonstrated that the membrane can be successfully actuated, further tests can focus on the dynamic response of the membrane. Micro PIV could be useful in visualizing and quantifying the jet field. It is hoped that once the successful operation and satisfactory performance of the jets are confirmed, the jets will be used to control some classic flows. Some possible flows to be studied include boundary layer plate flow or wake flow. The jet should also hold great promise as a mixer, particularly for gaseous flows.

REFERENCES

1. Bao, Z., Mukherjee, S., Roman, M. and Aubry, N., "Nonlinear vibrations of strings and membranes without tension", ASME Journal of Applied Mechanics 71(4), 551-559, 2004.

2. Bao, Z., Mukherjee, S., Roman, M. and Aubry, N., "Nonlinear Mechanics of MEMS Plates with a Total Lagrangian Approach." Computers and Structures. Volume 83, Issues 10–11, April 2005, pp. 758-768.

3. Blech, J.J., "On Isothermal Squeeze Films." *Journal of Lubrication Technology.* October 1983, Vol. 105, pp. 615-620.

4. Chanaud, R.C. 1994. "Effects of Geometry on the Resonance Frequency of Helmholtz Resonators." *Journal of Sound and Vibration.* Volume 178, No. 3., pp. 337-48.

5. Coe, D.J., M.G. Allen, B.L. Smith, and A. Glezer. 1995. "Addressable Micromachined Jet Arrays." Technical Digest: Transducers '95. Stockholm, Sweden.

6. Eaton, William P., Fernando Bitsie, James H. Smith, David W. Plummer. "A New Analytical Solution for Diaphragm Deflection and its Application to a Surface-Micromachined Pressure Sensor." Technical Proceedings of the 1999 International Conference on Modeling and Simulation of Microsystems. Chapter 17: Applications: Pressure, Actuation, Navigation, pp. 640-643.

7. Gad-el-Hak, Mohamed. 2000. *Flow Control: Passive, Active, and Reactive Flow Control Management*, Cambridge University Press.

8. Glezer, A. and Michael Amitay. 2002. "Synthetic Jets". *Annu. Rev. Fluid Mech.*, 34:503-29.

9. Glezer, A. et al. 1998. "Synthetic Jet Actuator and Application thereof." United States Patent, No. 5,758,823, Jun. 2, 1998.

10. Ingard, Uno. 1953. "On the Theory and Design of Acoustic Resonators." *The Journal of Acoustical Society of America.* Vol 25, No. 6, pp. 1037-1061.

11. Kovacs, G.A.T. 1998. *Micromachined Transducers Sourcebook.* New York: McGraw-Hill.

12. Mittal, R. et al. 2001. "Interaction of a Synthetic Jet with a Flat Plate Boundary Layer." AIAA Fluid Dynamics Conference & Exhibit, 31 st, Anaheim, CA, 2001, AIAA 2001-2773.

13. Muller, Michael O. et al. 2000. "Micromachined Acoustic Resonators for Microjet Propulsion." (2000) AIAA Paper 2000-0547.

14. Muller, Michael O. et al. 2000. "Thrust Performance of Micromachined Synthetic Jets." AIAA Paper 2000-2404.

15. Muller, Michael O. et al. 2000. "Flow Field and Performance of High Frequency Micromachined Synthetic Jets" AIAA Paper 2002-0974.

16. Rathnasingham, Ruben. September 1995. Coupled Fluid-Structural Characteristics of Actuators for Flow Control. MIT Master Thesis.

17. Rathnasingham, Ruben. June 1997. System Identification and Active Control of a Turbulent Boundary Layer. MIT Ph.D. Dissertation.

18. Rizzetta, Donald P., Miguel R. Visbal, and Michael J. Stanek. 1999. "Numerical Investigation of Synthetic-Jet Flowfields." *AIAA Journal*, Vol. 37, No. 8, pp. 919-27.

19. Senturia, Stephen D. 2001. *Microsystem Design*, Boston: Kluwer Academic Publishers.

20. Smith, Barton L and Ari Glezer. 1998. "The Formation and Evolution of Synthetic Jets." *Physics of Fluids*, Vol 10, No. 9, pp. 2281 – 97.

21. Steinberg, Dave S.. 1973. *Vibration Analysis for Electronic Equipment*, New York: John Wiley & Sons.

22. Timoshenko, S. and S. Woinowsky-Krieger. 1959. *Theory of Plates and Shells*, New York: McGraw-Hill Book Company.

23. Timoshenko, S. D.H. Young and W. Weaver, Jr. 1974. *Vibration Problems in Engineering*, 4th Ed., New York: John Wiley & Sons.

24. Ugural, Ansel C. 1999. *Stresses in Plates and Shells*, 2nd Ed., New York: McGraw-Hill.

25. Want, H. and S. Menon. 2001. "Fuel-Air Mixing Enhancement by Synthetic Microjets." AIAA Journal. Vol. 39, No. 12.

26. Ward-Smith, A.J., 1980. *Internal Fluid Flow: The Fluid Dynamics of Flow in Pipes and Ducts*, Oxford: Clarendon Press.

27. Williams, Kirt R. 1996. "Etch Rates for Micromachining and IC Processing." v 4.4, U.C. Berkeley Microfabrication Laboratory, Berkeley Sensor & Actuator Center.

28. Zengerle, R. and Martin Richter. 1994. "Simulation of Microfluid Systems." *J. of Micromech. Microeng*. Vol 4, pp. 192-204.

29. Zengerle, R. et al. 1995. "A Bidirectional Silicon Micropump." Micro Electro Mechanical Systems, 1995, MEMS '95, Proceedings. IEEE, 29 Jan-2 Feb 1995 IEEE pp. 19-24.